Energy Reports 11 (2024) 4085–4101

Contents lists available at ScienceDirect

Energy Reports

journal homepage: www.elsevier.com/locate/egyr

Research paper

Analysis of a stand alone battery-converter device from a simulative systems engineering perspective

Gerd Liebig [a,b,*], Stefan Geißendörfer [b], Frank Schuldt [b], Karsten von Maydell [b]

[a] Carl-von-Ossietzky University of Oldenburg, Institute of Physics, Carl-von-Ossietzky Strasse 9-11, D-26111 Oldenburg, Germany
[b] German Aerospace Center (DLR), Institute of Networked Energy Systems, Energy Systems Technology, Carl-von-Ossietzky-Straße 15, D-26129 Oldenburg, Germany

ARTICLE INFO

Keywords:
Advanced energy technology
Energy engineering
Thermal engineering
Lithium-ion batteries
Power converter
Battery management

ABSTRACT

A design analysis method for the concept of a modular battery pack based on physical modeling is presented, particularly for a prototype still under development. The originality of this work is threefold: A system engineering framework that aims to provide a process for design-based analysis. The construction of a modular battery system model and a focused examination on the technological implications of its design. This is achieved by a reliable assessment of the primary system components, the battery and dc-to-dc converter, proving consistency with recent insights from experiments and literature. The process is not limited to a specific design but can be applied to any battery system and serves as a starting point for further design optimization.

1. Introduction

Lithium-ion batteries (LIB) have gained high attention and are most promising to become a key enabler for sustainable development and climate neutrality on a global scale (Nations, 2015; Zubi et al., 2018; Poblete-Cazenave et al., 2021; Rojas et al., 2024). They can be used in modern energy services, i.e. grid support, voltage control, frequency regulation or e-mobility, as the technology enables much higher energy and power density as well as fast charging functionality compared to other existing battery technologies (Korthauer, 2013; Grey and Hall, 2020). However, LIBs lacking thermal stability and suitable performance requirements for their application in a battery system may fail early in their projected lifetime (Zhao et al., 2015; Khan et al., 2017; Arora, 2018). As battery cell and system demands from the application increase, system design and requirements engineering become more challenging (Saw et al., 2016; VDI/VDE, 2021; Frith et al., 2023).

To evaluate a battery design, you need to understand physical processes, data availability, modeling approach, numerical constraints and limitations to derive a proper strategy: The assessment of batteries involves geometrical (Zhao et al., 2015; Vega-Garita et al., 2017), electrochemical (Newman and Tiedemann, 1975; Jokar et al., 2016; Chen et al., 2020), electrical (Omariba et al., 2019; Geng et al., 2021), thermal (Bandhauer et al., 2011; Kim et al., 2013; Lundgren et al., 2015; Khan et al., 2017; Li et al., 2022; Chang et al., 2023; Ren et al., 2023) and mechanical (Marcicki et al., 2017; Arora, 2018; Epp and Sauer, 2021; Xi et al., 2022) dependencies, a multiphysical problem. While previous studies often focus on evaluation methods, the broader engineering implications are often overlooked. Achim et al. (2022) emphasize the challenges in battery system design due to versatile components and functional correlations. Existing product structures lack flexibility and adaptability for future battery designs. They recommend a generic domain-based product architecture to simplify and structure product design architectures. However, an actual implementation and validation are still required. Madani et al. (2023) did a review study on the thermal properties and effects of battery thermal management systems (BTMSs). They came to the conclusion that an accurate battery model is needed for the best performance and safety analysis of lithium-ion batteries. Stand-alone thermal models are not accurate. Instead, electrochemical, electrical, and thermal aspects must be coupled. Astaneh et al. (2022) developed a multiphysics simulation optimization framework specifically for lithium-ion battery pack design in electric vehicles. Their work acknowledges the need for such a framework during early cell design, where research on cell-to-pack interactions is limited. However, it is important to note that their study primarily focuses on parameter optimization, without extensively exploring broader system implications. Every research group highlights the importance of adopting a structured approach to formulate design

* Corresponding author at: German Aerospace Center (DLR), Institute of Networked Energy Systems, Energy Systems Technology, Carl-von-Ossietzky-Straße 15, D-26129 Oldenburg, Germany.

E-mail addresses: gerd.liebig@uni-oldenburg.de, gerd.liebig@dlr.de (G. Liebig), stefan.geissendoerfer@dlr.de (S. Geißendörfer), frank.schuldt@dlr.de (F. Schuldt), karsten.maydell@dlr.de (K. von Maydell).

https://doi.org/10.1016/j.egyr.2024.03.053
Received 2 January 2024; Received in revised form 15 March 2024; Accepted 26 March 2024
Available online 8 April 2024
2352-4847/© 2024 The Author(s). Published by Elsevier Ltd. This is an open access article under the CC BY license (http://creativecommons.org/licenses/by/4.0/).

recommendations, particularly during early development when not all constraints are fully understood. Hence, in the present work, a straightforward, simple simulative engineering framework is addressed to provide practical engineering tips.

Before solving a problem, make sure you know what you need to achieve: Schlick et al. (2012) stated that the high cost of battery development and production compared to the low sales volume makes electrification unlikely for many applications. Due to economies of scale, modular system topologies based on standardized subunits could improve application diversity. Rothgang et al. (2015) stated that a modular battery system connected to a combined link via dc-to-dc converters would allow for greater flexibility in system design while improving durability and safety. Power converters must be highly efficient and reliable (Dokić and Blanuša, 2014; Sutikno et al., 2023). However, in practice, converter efficiency ranges from 70 to 95% (Severns and Bloom, 1985; Alatai et al., 2021). In the present work within the research project BaSyMo (Zahid, 2018; Liebig et al., 2019a), the ideas are merged and the following design is examined: "A modular battery system design with a dc-to-dc converter within one block. Each block should be voltage-controlled, meet application-oriented electrical requirements, and easily fit energy demand by adding blocks".

To generate promising system design decisions, it helps to look at existing solutions: Reiter et al. (2019) advised simulating subsystems with quick computing, efficient parameterization, and high precision to develop a reliable system concept. In other words, the simulated system design behavior can be understood on the basis of simpler benchmark models that are already validated in a broader operation scope. In previous studies (Liebig et al., 2019b, 2020) we conducted experiments and simulations on the same prismatic battery that is considered in the design evaluation to study its electrochemical and thermal behavior under static and dynamic conditions. Several studies (Kim et al., 2013; Li et al., 2022; Chang et al., 2023; Ren et al., 2023; Xi et al., 2022) analyzed the relationship between temperatures, heat generation, heat dissipation and operation modes by means of an established electrochemical-thermal coupling model for prismatic-type battery cells and/or packs under varying operation conditions. Hence, in the present work, these studies are utilized as benchmarks to interpret battery behavior with influence from the dc-to-dc converter.

In view of the above, the aims of this work are:

(I) To provide a simulative design engineering framework for virtual assessment of a lithium-ion battery system to support the design research at limiting conditions in the early phase of development.
(II) To carry out a reliable assessment of the primary system components, the battery and dc-to-dc converter, and prove consistency with recent insights from experiments and literature.
(III) To demonstrate the thermal evaluation of the BaSyMo design to understand the effects of the temperature dynamics of its key components and their system-level consequences.

The remainder of the paper is organized as follows: For (I), the methodological approach is described in Section 2 in detail to realistically be reproduced in Section 3 during its application to the BaSyMo design. For (II), the models are set up in Section 3 and their verification is addressed in Section 4. For (III), in Section 3, two use-cases are presented based on actual application conditions, analyzing the feasibility of the design variants. A conclusion is presented in Section 5.

2. Methods - Mathematical modular battery system model

The systematic framework proposed in Table 1 is to solve the above product design problem with the support of simulation equipment.

The methodology is meant to offer general guidance for decision-making during design evaluation within five steps, especially with a focus on the demanding challenges of a modular battery system design. In step 1, the principle design and technical requirements are identified as design constraints. From this, a base-case design is generated, and available physical settings are identified. In step 2, the main performance characteristics, operation limits and hotspots of the main functional units are identified. In step 3, the base-case model is built and performance metrics are collected. To improve the hotspots, a few design targets and alternative designs are generated in step 4.

2.1. Step 1: Identify the principle system design and technical requirements and generate the base-case design

Consumer preferences need to be translated into a set of technical requirements by using a knowledge base and heuristics. The requirements can be physical properties (mechanical, electrochemical, thermal, etc.), functional performance, or product characteristics. To ensure high product quality, the design constraints for the technical requirements should be specified as depicted in Table 2.

The logic follows requirements necessarily fulfilled by cell, conventional systems, or modular system design choices and contains an intrinsic hierarchy. Each of the corresponding design targets is interesting to evaluate within the system design development. The overview shows that system properties with an electrochemical energy storage background are mostly already predetermined by the selection of the cell type. This work focuses on a modular battery system design. Hence, we are primarily interested in how the additional design requirement for a modular system influences the already existing system characteristics.

As a reference, a base-case product is presented that meets the principle design specifications. Generally, this can be an existing product, but for a prototype, it must be developed based on brainstorming, technical know-how, heuristics, and marketing experience (Seider et al., 2017; Zhang et al., 2020). While the general functional design could be independent of physical properties, a specific base-case design is usually based on a fixed set of design parameters.

For the module design in mind power conversion and flexibility requirements within the base-case design are taken care of by using four integrated dc-to-dc converter in combination with a battery pack, i.e. 12 battery cells in series connection. The electrical circuit representation as principle design and a mockup unit, a full size design model of the device used for demonstration, are shown in Fig. 1.

Results of the base-case design evaluation are shown in Section 3.1.

2.2. Step 2: Identify the main performance characteristics for the principle components

In this section, the system requirements and main performance characteristics are analyzed. At an early stage in development, usually no or insufficient performance and operational data are available for the main components, so property data must be collected through experimental characterization methods or literature research.

From the systems perspective, the battery cell and converter need to fulfill the spatial and electrical design requirements, while temperature safety is ensured at each operation state. Simply put, all the battery cell data is suitable for the basic design that accommodates the prismatic format of the PHEV2, while the electrical properties fit the operating range of the converter prototype. The battery type chosen in this study is a prismatic PHEV2 type with a NMC-based positive electrode and a graphite-based negative electrode material. Electrical properties comprise a nominal capacity of 40.0 Ah, a cell potential of 2.8 V to 4.2 V, and maximal allowed continuous current of 5.0 C during charge, and continuous current of 10.0 C during discharge operation. According to the manufacturer, the battery cell temperature is allowed to reach 45 °C during charge operation and 65 °C during discharge operation. Even though, safety limits are maintained throughout the lifetime, cell operation at elevated temperature, elevated current, and/or low

Table 1
Key steps of methodology.

1.	Identify principle system design and technical requirements and generate a base-case design.
2.	Identify the main performance characteristics (dependent on each component) and operation limitations through, • experimental data from measurements and corresponding model development, • validated physics-based model from the literature.
3.	Build a base-case model design and evaluate metrics at hotspots (stages of major impact) through technological case studies, i.e.: • combinatorial or functional estimation of component units within the system. • estimation of components for various operation conditions.
4.	Generate design targets and alternative designs through the translation of system behavior into design metrics (i.e. power, durability and safety) and repeating methodology.

Table 2
Requirements for the battery system designs (Cell C, System S, Modular M).

Criteria	Description	Constraint
Cell design		
Safety	The Possibility of a critical safety hazard by the cell is low.	C
Energy	The energy provided by the cell meets the user's demand.	C
Power	The power provided by the cell meets user demand.	C
Durability	The cell lifetime meets the application requirement.	C
Cost	Low battery material resource and availability cost.	C
Fast charge	Capability for the cell to be charged in fast times.	C
Conventional system design		
Safety	The components run within safety margins. and catastrophic events are avoided.	S
Power	The system operates at high efficiency and provides stable power at all system states.	S
Durability	The service lifetime fulfills optimal cell life conditions. The influence of temperature on the aging of the cells is monitored and moderated by the system.	S
Cost	The system is reasonably priced compared to cell costs.	S
Reliability	The system performs reliable during service lifetime. This includes dust-, water- and air-tight as requirement.	S
	Cooling mechanisms within a BTMS might be available.	S
Easy-to-use	The system should easily be installed and maintained within the application.	S
Modular system design, i.e. BaSyMo		
Safety	Thermal runaway can be captured within one module, and components act thermally negligible towards each other.	M
Easy-to-use	An average person should be able to transport and connect the module between various applications. Hence, the module should not weigh too much and the weigh should be evenly distributed among its volumes.	M
Flexibility	The output voltage adjustment utility is effect-neutral versus battery service-lifetime.	M

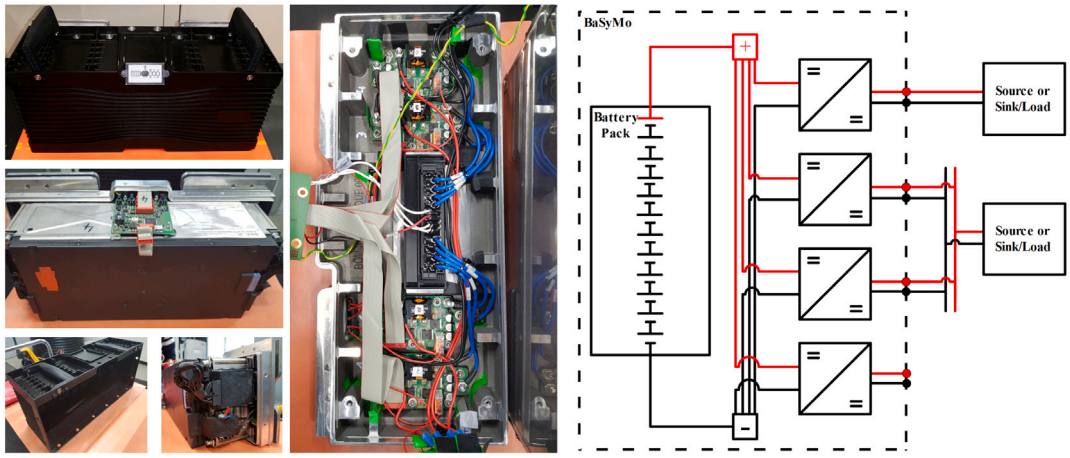

a) Prototype dummy with base-case design **b)** Principle design as electrical diagram

Fig. 1. (a) Several perspectives on the base-case design and (b) Exemplary electrical diagram of the prototype during operation, while connected to a device on one channel, paralleled on a device with two additional channels, and idle at the last channel, where each device-connection could be configured on their own voltage level, and the dotted line resembles the system casing.

and high SoC conditions for a long duration might lead to decreased durability (Smith et al., 2016; Keyser et al., 2017).

For the module flexibility purpose, a dc-to-dc converter has been developed, that is based on the LT8708 chip from the manufacturer Linear Technology/Analog Devices (California, United States of America), a high-performance synchronous 80 V four-switch Buck-Boost dc-to- dc controller with flexible bi-directional capability (Linear Technology/Analog Devices, 2018). The maximal electrical output current per converter is designed to be 20 A, hence, translating to a maximal current output of 80 A of the system and a maximal power output of 4.8 kW of the system in relation to 60 V output voltage. To increase the strength of the housing and to protect the converters from mechanical and thermal shocks, the back of the module in which the converters are integrated is made of metal. The rest of the casing is made of plastic. A control unit and a display are mounted on top of the module. The component placement and casing design are meant to be symmetrical towards the center of the battery to ensure even weight distribution.

Results of the component assessment are discussed in Section 3.2.

2.3. Step 3: Build base-case model design

The model variants are based on the finite-element method (FEM) and implemented in the COMSOL Multiphysics® v5.6 (Stockholm, Sweden) simulation platform using the lithium-ion battery submodule for the definition of the electrochemical behavior of the battery cells and system components and the heat transfer in solids and fluids submodule to describe the thermal behavior within the system environment with respect to fluid flow conditions provided by the laminar flow submodule. Throughout the operation scenarios, the governing equations of the models are computed in a transient and spatially resolved manner. At first the model equations are described with respect to their physical nature. Then, the model layout including the positions of the boundary conditions, is presented.

Heat transfer in Solids: The heat propagation within solid domains $V \subset \mathbb{R}^3$ at position $s = (x, y, z) \in V$ and time $t \in \mathrm{T} = [0, \tau]$, $\tau > 0$, is calculated by the transient heat transfer equation. Domains emitting heat are denoted with regard to the battery cells' electrode stacks by $V_{stack} = \bigcup_{k\in K} V_{stack,k}$, $k \in K$, and the converter by $V_{conv} = \bigcup_{i\in I} V_{conv,i} = \bigcup_{i\in I}\bigcup_{j\in J} V_{conv,ij}$, $i \in I$, $j \in J$, for the ith dc-to-dc converter and its jth component. The equations are depicted as follows:

$$\underbrace{\rho C_p \frac{\partial \vartheta}{\partial t}}_{\text{Diffusion}} + \underbrace{\rho C_p \nabla \cdot (k \nabla \vartheta)}_{\text{Conduction}} = \underbrace{\begin{cases} Q_k\left(s, \vec{Z}_{stack,k}\right), & s \in V_{stack,k} \\ Q_{ij}\left(s, \vec{Z}_{conv,i}\right), & s \in V_{conv,ij} \\ 0 & , s \notin V_{conv} \cup V_{batt} \end{cases}}_{\text{Heat Source}} \tag{1}$$

where $\vartheta : \mathrm{T} \times V \to \mathbb{R}$ is the temperature, $Q_k : V_{stack,k} \times \mathbb{R} \times \mathbb{R} \to \mathbb{R}$ is the heat dissipation density dependent on the state vector $\vec{Z}_{stack,k} = [\vartheta_{avg,k}, I_{pack}]$, while $Q_{ij} : V_{conv,ij} \times \mathbb{R} \times \mathbb{R} \times \mathbb{R} \times \mathbb{R} \to \mathbb{R}$ is the heat dissipation density dependent on the state vector $\vec{Z}_{conv,i} = [I_{pack}, U_{pack}, I_{out,i}, U_{out,i}]$, where $\vartheta_{avg,k} : \mathrm{T} \times V_{stack,k} \to \mathbb{R}$ is the volumetric average electrode stack temperature within the kth stack $V_{stack,k}$, $I_{pack} : \mathrm{T} \to \mathbb{R}$ is the battery pack current, $U_{pack} : \mathrm{T} \to \mathbb{R}$ is the battery pack voltage, $I_{conv,i} : \mathrm{T} \to \mathbb{R}$ is the ith dc-to-dc converter output current and $U_{conv,i} : \mathrm{T} \to \mathbb{R}$ is the ith dc-to-dc converter output voltage. The material properties are $\rho : V \to \mathbb{R}$ density, $C_p : V \times \mathbb{R} \to \mathbb{R}$ temperature-dependent specific heat capacity under constant pressure, and $k : V \times \mathbb{R} \to \mathbb{R}^{3\times 3}$ thermal conductivity.

Heat transfer in Fluids: The heat propagation within the fluid domains $F \subset \mathbb{R}^3$ surrounding the battery system components is considered at position $s = (x, y, z) \in F$ and time $t \in \mathrm{T} = [0, \tau]$, $\tau > 0$, as follows:

$$\underbrace{\rho C_p \frac{\partial \vartheta}{\partial t}}_{\text{Diffusion}} + \underbrace{\rho C_p \vec{u}\, \nabla \vartheta}_{\text{Advection}} - \underbrace{\nabla \cdot (k \nabla \vartheta)}_{\text{Conduction}} = 0 \tag{2}$$

where $\vartheta : \mathrm{T} \times F \to \mathbb{R}$ is temperature, $\rho : F \times \mathbb{R} \to \mathbb{R}$ is density, $C_p : F \times \mathbb{R} \to \mathbb{R}$ is specific heat capacity under constant pressure and $k : F \times \mathbb{R} \to \mathbb{R}^{3\times 3}$ is the thermal conductivity matrix. The vector $\vec{u} : F \to \mathbb{R}^3$ describes air-stream velocity within the fluid domain F.

Fluid Dynamics: The environment surrounding the battery system parts is modeled with stationary equations of both momentum balance Eq. (3) and continuity Eq. (4), to replicate the weakly compressible fluid flow behavior within the fluid domain $F \subset \mathbb{R}^3$ representing air:

$$\rho \left(\vec{u} \cdot \nabla\right) \vec{u} = \nabla \cdot \left[-pI + \underbrace{\left[\mu\left(\left(\nabla \vec{u} + \left(\nabla \vec{u}\right)^T\right) - \tfrac{3}{2}\left(\nabla \cdot \vec{u}\right) I\right)\right]}_{\text{Weakly Compressible Flow}}\right] \tag{3}$$

$$\nabla \cdot \left(\rho\, \vec{u}\right) = 0 \tag{4}$$

Therein, $\rho : F \times \mathbb{R} \to \mathbb{R}$ is density and $\mu : F \times \mathbb{R} \to \mathbb{R}$ is dynamic viscosity; both are calculated in dependence of constant external temperature ϑ_{ext}. The vector $\vec{u} : F \to \mathbb{R}^3$ is airstream velocity, $p : F \to \mathbb{R}$ is the pressure variable and I is the identity matrix.

On each boundary S the temperature ϑ is defined as follows: $\vartheta : \mathrm{T} \times S \to \mathbb{R}$. The energy and fluid flow through boundaries are defined and scaled based on the normalized orthogonal vector $\vec{n} : S \to \mathbb{R}^3$, as well as the weighted temperature gradient $k\nabla\, \vartheta$, both associated with the local boundary S.

Convection: The heat transferred via convection is considered on a boundary $S = \partial V \subset \mathbb{R}^2$ of a solid volume $V \subset \mathbb{R}^3$ pointwise for $s \in S$ by the following Robin condition:

$$-\vec{n} \cdot k\nabla\, \vartheta = h_S\left(\vartheta - \vartheta_{ext}\right) \tag{5}$$

Therein, h_S = const. is the convective heat transfer coefficient at the boundary S and ϑ_{ext} = const. is the temperature of an external domain. This boundary condition applies to the thermally isolated ground of the battery system module. Elsewhere, convection on battery system surfaces is implicitly defined by interactions with a surrounding fluid domain.

Radiation: The heat transferred by radiation is considered on a boundary $S = \partial V \subset \mathbb{R}^2$ of a solid volume $V \subset \mathbb{R}^3$ pointwise for $s \in S$ by the following Robin condition:

$$-\vec{n} \cdot k\nabla\, \vartheta = \sigma \epsilon_S\left(\vartheta^4 - \vartheta_{ext}^4\right) \tag{6}$$

where σ is the Stefan–Boltzmann constant, $\epsilon_S : S \to \mathbb{R}$ is emissivity and ϑ_{ext} = const. is the external environment temperature. This condition is applied to battery system surfaces facing a fluid domain.

Open Boundary: Open boundaries S_{open} are defined in the heat transfer and fluid flow models by conditions on the velocity vectors $\vec{u}$ and $\vec{n}$ for $s \in S_{open}$. In the thermal model, the conditions are simulated as follows: vspace-0.25 cm

$$\begin{cases} \vartheta = \vartheta_{ext} & \text{if } \vec{u} \cdot \vec{n} < 0 \\ -\vec{n} \cdot k\nabla\vartheta = 0 & \text{if } \vec{u} \cdot \vec{n} \geq 0 \end{cases} \tag{7}$$

In the fluid model, the normalized orthogonal velocity vector $\vec{n}, s \in S_{open}$ is adjusted as follows:

$$\left[-pI + \left[\mu\left(\left(\nabla \vec{u} + \left(\nabla \vec{u}\right)^T\right) - \frac{3}{2}\left(\nabla \cdot \vec{u}\right) I\right)\right]\right] \vec{n} = f_0 \vec{n} \tag{8}$$

where f_0 = const. is the stress associated with the open boundary. In this context, zero stress is selected for all model research situations, signifying the absence of external velocity field-induced stress.

Symmetry: Symmetry boundaries within the heat transfer and fluid flow models are denoted by S_{sym}. In the thermal model, the condition is simulated as follows:

$$-\vec{n} \cdot k\nabla\vartheta = 0 \tag{9}$$

In the fluid model, an adjustment on $\vec{u}$ and $\vec{n}, s \in S_{sym}$ is done as follows:

$$\begin{aligned} \vec{u} \cdot \vec{n} &= 0 \\ K_{\vec{n}} \cdot \left(K_{\vec{n}} \cdot \vec{n}\right) \vec{n} &= 0 \\ \text{where} \quad K_{\vec{n}} &= \left[\mu\left(\left(\nabla\vec{u} + \left(\nabla\vec{u}\right)^T\right) - \tfrac{3}{2}\left(\nabla \cdot \vec{u}\right) I\right)\right]\vec{n} \end{aligned} \tag{10}$$

Inlet Fluid Flow: This model is intended to mimic the climate chamber fan effect on the flow of fluid towards the battery system from the boundary S_{in}. This is done by adjusting the normalized orthogonal velocity vector $\vec{n}, s \in S_{in}$:

$$\vec{n} = -V_{in}\vec{n} \tag{11}$$

where V_{in} = const. is the inlet velocity control parameter. The velocity is chosen based on the model study environment conditions.

Outlet Fluid Flow: The outlet of the fluid flow field is simulated opposite to the inlet at the boundary S_{out} by adjusting the normalized orthogonal velocity vector $\vec{n}, s \in S_{out}$:

$$\left[-p(s)\, I + \left[\mu\left(\left(\nabla\vec{u} + \left(\nabla\vec{u}\right)^T\right) - \frac{3}{2}\left(\nabla \cdot \vec{u}\right) I\right)\right]\right]\vec{n} = -p_0\vec{n} \tag{12}$$

where p_0 = const. is the pressure associated with the outlet velocity. In this context, all model study cases are conducted at atmospheric pressure, and backflow of fluid is prevented. This condition maintains the direction of the fluid flow at the outlet.

Coupling of Physics: By the Eqs. (1) to (2), the thermal behavior of the battery system and its components can be calculated in dependence of the heat generated within the electrode stack and the converter components, while simultaneously exchanging the average temperature of the battery packs electrode stacks ϑ_{ave} with the electrochemical cell submodel. The Eqs. (2) and (3) are one-way coupled to the velocity term u due to the fact that a stationary fluid flow is computed in the exterior domain of the battery building block of the temperature distribution before the transient calculation. Hence, work induced by velocity or pressure changes due to temperature variation of air can be neglected, although air density is still temperature-dependent in Eq. (2). Furthermore, buoyant flow generated by a temperature-dependent air density within the framework of gravitational fluid force is disregarded. The simplification is justified by the presence of a predominant flow field and increased conduction along solid domains that are very thermally conductive, like steel and copper.

The behavioral system simulation is performed with respect to the electric diagram shown in Fig. 1. Kirchhoff's law of electro-circuit is used for the cell currents and voltages, together with the following energy conversion relations: $P_{out} = \eta P_{in}$ and $P = IU$, which hold true for the main circuit and each electrical component's subcircuit. The following set of equations are solved as ordinary differential equations for time $t \in \mathrm{T} = [0, \tau]$, $\tau > 0$, where $P_{sys,app}$ is the total applied system power, $P_{app,i}$ is the applied power of the ith converter, and P_{batt} is the battery power, each with respective current and voltage variables:

$$P_{sys,app} = \sum_{i \in I} P_{app,i} = \sum_{i=1}^{4} I_{app,i} U_{app,i} \tag{13}$$

$$P_{batt} = \sum_{i \in I} P_{conv,i,in} = \sum_{i \in I} \frac{P_{conv,i,out}}{\eta_{conv,i}} = \sum_{i=1}^{4} \frac{I_{app,i} U_{app,i}}{\eta_{app,i}} \tag{14}$$

$$I_{batt} = \frac{P_{batt}}{U_{batt}} = \frac{P_{batt}}{\sum_{k \in K} U_k\left(\vartheta_{avg,k}\right)} = \frac{P_{batt}}{2\left(U_1\left(\vartheta_{avg,1}\right) + \cdots + U_6\left(\vartheta_{avg,6}\right)\right)} \tag{15}$$

where the Eqs. (13) to (15) manage energy balance, while Eq. (15) is used as input for electrochemical submodels of each electrode stack within the battery pack. Thus, thermal influences on the cell voltage and heat generation rate of each battery cell are considered. Therein, the cells have the same current in the series connections, and the total pack voltage is the sum of the voltages passing through each cell (Yang et al., 2022). This model simplification is radical in comparison to the real physical system; however, the coupling provides a practical first approach. The coupling remains feasible for brief simulation periods at the level of individual batteries, provided that the temperature variation within the electrode domain is negligible (Lundgren et al., 2015). In general, the coupling is a matter of research since it has a huge impact on heat propagation patterns within the cell model, especially with regard to the highly thermally conductive layer and the terminals (Liebig et al., 2020; Queisser et al., 2021). Battery pack simulation results are expected to be more realistic with short simulation duration times and lower temperature nonuniformity.

Heat generation: Instead of a fully reduced behavioral model on system level, a spatially resolved thermal model is preferred in this work, since direct heat emitted from the converter array is of interest. Each electrode stacks average volume temperature and the battery pack current are used to solve for separate heat generation rates $Q_k, k \in K$; coupling is as depicted in the Eqs. (1) and (15). Main heat loss at the converter components originates from inside of the components. Therefore, a volumetric heat generation density Q_{ij} is considered for the ith converter and its jth component as follows:

$$Q_{ij} = \left(\frac{I_{app,i}}{I_{app,i,max}}\right) Q_{i,j,max}, i \in I, j \in J \tag{16}$$

where the maximal simulated heat generation density $Q_{i,j,max}$ of the ith converter and jth board component is scaled by the ratio of the provided $I_{app,i}$ and maximal $I_{app,max}$ output current measured in the characterization experiment at the examined converter operation state. The experimental and simulative look-up table data is provided in Appendix A.2. The Eq. (16) is spatially coupled to Eq. (1).

The schematics of the system model implementation and the layout of the battery system model are illustrated from several perspectives in Fig. 2.

2.4. Step 4: Generate design targets and potential alternative designs

Various product design targets can be proposed to improve design hotspots. Indeed, the first step is to identify the information needed rather than get a detailed design solution. This is important because most relevant data is often not available for LIBs, but important design choices can be made even in the absence of data. In this work, the following alternative variants are examined:

- Cell material matters: The basic design is defined with a NMC cathode-type battery cells. What would be different if LFP material were used instead?
- Flexibility as an Option: Applications might use the SoC-dependent voltage feedback of a battery and control the current accordingly. What would be the thermal implications of using the battery without the converter?

The task is to decide on the physical model design. Through the modeling of chosen technological use-cases, performance metrics can be quantified, and hotspots identified. The electrode, cell and converter submodel are the best ways to sort and rate different BaSyMo module designs based on how well their parts work.

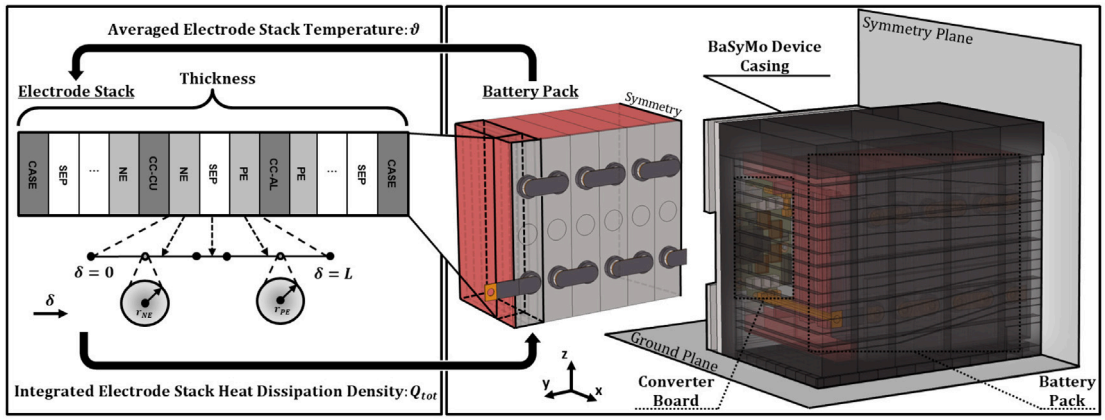

a) Schematics of the lithium-ion battery and heat transfer cfd system model

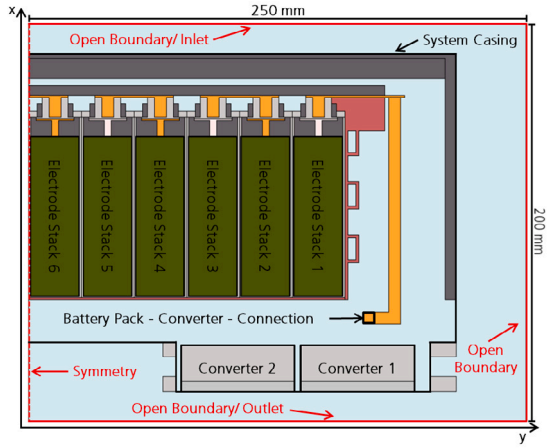

b) Battery pack perspective

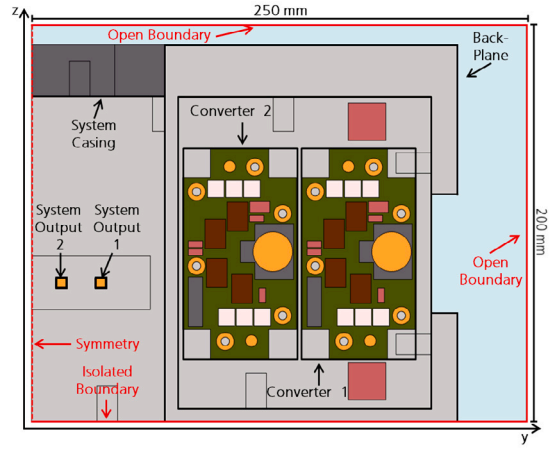

c) Back-plane perspective

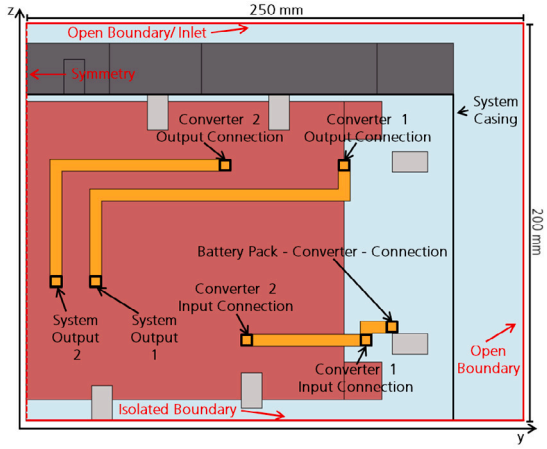

d) Connections perspective

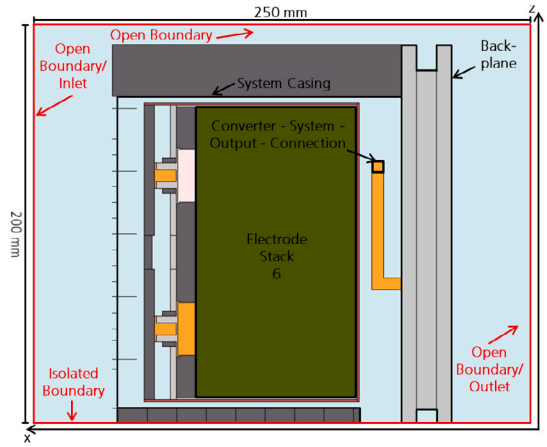

e) Battery six perspective

Fig. 2. (a) Schematics of the system model and several 2D perspectives of the base-case design at (b) the battery pack: yx-plane at $z = 85.0$ (mm), (c) back-plane: mixed parallel yz-planes at $x = \{116.50, 121.50, 141.50\}$ (mm), (d) connections: yz-plane at $x = 153.50$ (mm) and (e) battery six: xz-plane at $y = 13.25$ (mm).

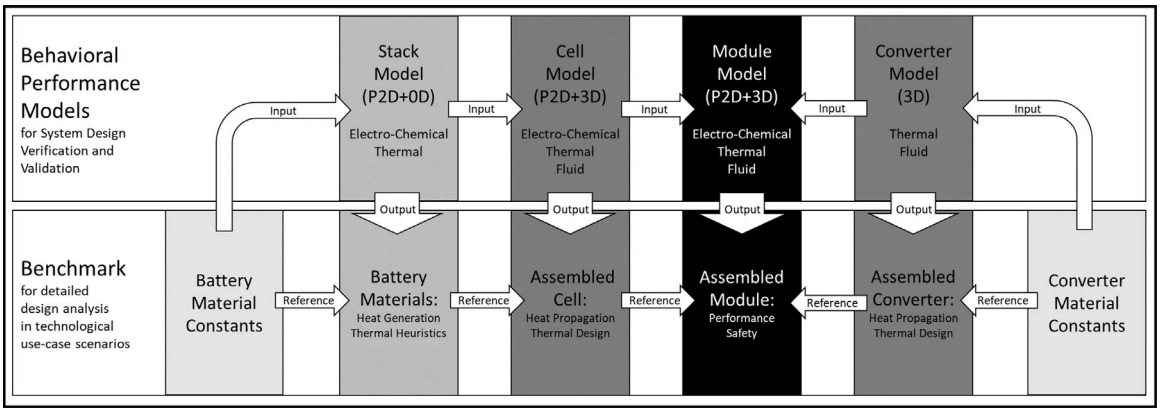

Fig. 3. Multiscale and multi-physics battery and converter model hierarchy for module design analysis with submodel benchmarks.

The hierarchical structure in the present battery system model design and the associated model plausibility levels are illustrated in Fig. 3.

3. Results and discussion

System design requirements are evaluated with respect to cell, conventional system and BaSyMo specific characteristics, as defined in step 1. In step 2, performance characteristics of the converter and battery are evaluated and components models are build. In step 3, the base-case model is evaluated in relation to worst-case conditions. Finally, the possible benefit by an active BTMS as alternative design variant under the compromise of additional cost is evaluated and compared to the base-case result in step 4. The reader is referred to Section 4 for model verification of the battery, converter and the battery system in separate settings.

3.1. Step 1: Principle system design evaluation - Why cell material matters

The aim of comparing relative design quality criteria is to show how the framework can be used to efficiently identify the information needed for designing a product, rather than getting a detailed design solution. The data can be considered a starting point for further system rating since an ideal system preserves power, energy, durability and cost at the cell level, while safety and fast charge could be enhanced at the system level. It is well known that using LFP material, instead of NMC material, the safety risks are decreased, however, energy density is compromised (Brand et al., 2013; Graf, 2018). Easy-to-use and flexibility are projected to improve in the base-case design in comparison to conventional systems independent of the same cell material type. Furthermore, the need for power electronics increases cost, but BTMS could be simplified, when the base-case design without active cooling operates within the allowed temperature window by the manufacturer. Implications on safety, power and durability criteria are examined in more detail with respect to the thermal implications of the model study in technologically relevant operation scenarios. The starting point of the design evaluation is shown in Fig. 4 that summarizes attributes in this study with respect to a focus on cell and system design; scaling based on Refs. Hautier et al. (2011) and Graf (2018).

3.2. Step 2: Evaluate the limiting principle component characteristics

The characteristics of the principal components, the dc-to-dc converter and battery, are translated by experimental characterization into performance prediction models in this section. The dc-to-dc converter prototype is based on metal–oxide–semiconductor field-effect transistors (MOSFETs). The thermal performance of the dc-to-dc converter is measured within the experimental study to examine thermally significant hotspots and component limitations with respect to maximum temperature restrictions and their influence on the model replication and system limitations. The battery cell data considered in this work is referenced from previous work (Liebig et al., 2019b, 2020). A battery model is established based on characterization experiments and separate validation scenarios in hierarchical physical model depth. The reader is referred to Section 4 for more details on the battery model validation.

The voltage level U_{batt}, which corresponds to the battery pack, is modulated by a H&H NL1V80C40 dc-source/sink. The voltage level U_{app}, which represents the application, is modulated by a Delta Electronica SMK15K Series dc-source/sink. Flow of Current is direction dependent when measured. A negative current on either side of the converter means that energy is leaving, while a positive current means that energy is entering the converter. Thus, from the converter's point of view, a negative current I_{batt} corresponds to the charging process of the battery pack, while a positive current I_{batt} corresponds to the discharging process of the battery pack. The electrical values are measured with a time resolution of 1 s. The converter efficiency is calculated based on the absolute input and output power ratio, while the converter heat loss is calculated as absolute difference between input and output power. The constant current mode of the dc-to-dc converter is utilized to illustrate its electrical performance. The constant current mode employs a U_{batt} = 30 V input voltage and output voltages ranging from U_{app} = 10 V to 50 V with resolution U_{step} = 10 V, respectively. This configuration represents known applications spanning from 12 V to 48 V. A variation of the voltage U_{batt} is not presented, since the efficiency of the converter is modeled as battery voltage independent.

The tests of the converter board are performed within a Vötsch climate chamber VC 7018 within an allowed temperature range of −75 °C to 180 °C, which is temperature regulated by air circulation. The tests of the converter board are performed within a Vötsch climate chamber VC 7018 within an allowed temperature range of −75 °C to 180 °C, which is temperature regulated by air circulation. Assuming the climate chamber remains tightly sealed throughout operation, the thermal influence from the exterior are considered to be negligible. Furthermore, to mitigate the effects of uncertain reflected heat radiation, the inner chamber surfaces are clad in black molton, and to increase surface emissivity, the surfaces of the dc-to-dc converter are painted with a non-electrically conductive substance. The infrared temperature image of the converter object and its attached cooling block is captured by a Flir AX8 thermography camera. An Agilent 34 972A with three PT100 sensors, having a −40 °C to 85 °C (±0.1 K accuracy) temperature range each, is used to measure the temperature pointwise. The locations right next to the converter board, as well as the back side of the attached cooling block, are chosen to evaluate transient temperature readings. All temperature measurements are taken with

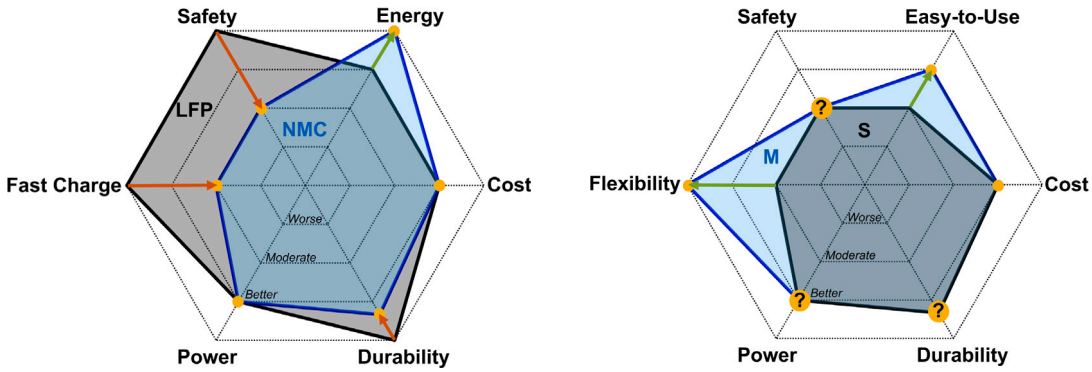

a) Starting point: Cell impact

b) Intermediate step: System influence

Fig. 4. (a) Relative impact of LFP and NMC positive electrode material choice on the system performance and (b) base-case design in relation to a system based on a Graphite-NMC cell type.

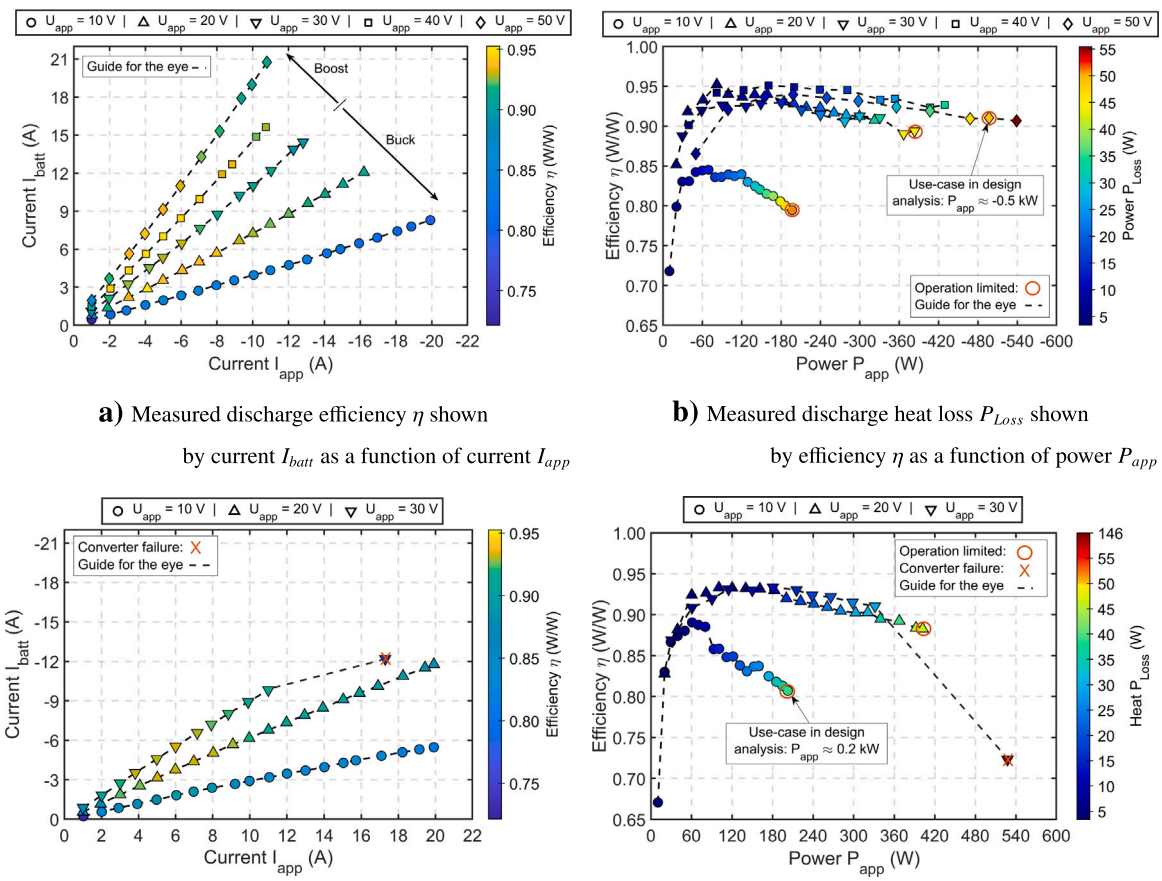

a) Measured discharge efficiency η shown by current I_{batt} as a function of current I_{app}

b) Measured discharge heat loss P_{Loss} shown by efficiency η as a function of power P_{app}

c) Measured charge efficiency η shown by current I_{batt} as a function of current I_{app}

d) Measured charge heat loss P_{Loss} shown by efficiency η as a function of power P_{app}

Fig. 5. Measured electrical and heat loss of the converter at U_{batt} = 30 V battery voltage, simulating a battery pack at a fixed SoC, during discharge ((a), (b)) and charge operation ((c), (d)).

a time resolution of 10 s. The increase in stationary temperature is measured at each use-case scenario within a current load ramp from 1 A to 20 A, step-wise by 5 A rise. If no temperature change occurs for at least twenty minutes in a current step, the average temperature value of the last five minutes is used as the performance log.

Electrical efficiency and heat loss results are shown with respect to use-case scenarios during charge and discharge operation in Fig. 5.

During charge operation, the battery current I_{batt} varies within the range above −0 A to −10 A, the stable applied power P_{app} varies within the range above 0 W up to 400 W, and the efficiency varies up to 93%. During discharge operation, the battery current I_{batt} varies within the range of 0.25 A up to 21 A, the applied power P_{app} varies within the range of −1 W up to −550 W, and the efficiency η varies up to 95%. When the performance of the converter becomes thermally or

Table 3
Power and temperature characteristics during stationary thermal test evaluation.

Use-case scenario	Battery power	Applied power	Electrical efficiency	Surface temperature centered at back-plane	Surface temperature at casing close to battery port	Surface temperature at casing close to applied port
	P_{batt} (W)	P_{app} (W)	$\eta(1)$	T (°C)	T (°C)	T (°C)
Discharge boost	552.3 ± 12.8	−503.6 ± 12.0	0.91 ± 0.01	33.4 ± 0.2	29.2 ± 0.23	30.6 ± 0.1
Charge buck	−162.4 ± 1.09	201.8 ± 15	0.80 ± 0.01	32.8 ± 0.1	25.90 ±0.17	28.7 ± 0.1

electrically unstable, operation is halted. The stable applied current I_{app} window decreases with increasing voltage U_{app} in both energy transfer directions. Performance results with respect to a 60 V applied voltage level could not be provided due to the lack of stable operation. The maximum efficiency in both scenarios is reached in the first third of the applied current range. Efficient operation above 90% is achieved with restrictions to operation modes $|I_{app}| > 2$ A and $U_{app} > 20$ V. The maximal applied power achieved during discharge operation was −550 W with a heat loss of around 55 W. Based on the electrical efficiency, each applied voltage-oriented operation mode has a restricted optimal applied output current. While the current levels are almost similar, when the battery and applied voltage levels are equal, there is an antiproportional trend during the buck and the boost operations. This trend is accompanied by a more stable efficiency of roughly 90% independent of the energy transfer direction at each evaluated applied current level when the battery and applied voltage equal, while a decrease in efficiency at low and high current levels is more pronounced when an offset between the battery and applied port is present. Less efficiency is accompanied by increased heat generation, which thermally limits the applied power of the converter due to the passive thermal design. Hence, active cooling could enhance the maximal applied power for the present design.

Table 3 shows the average result of transient temperature sensor measurements on local spots of the cooling block below the converter board along the electrical configuration data.

Six temperature evaluation spots (sp1) to (sp6), as well as an evaluation frame (box) of the dc-to-dc converter prototype, each emphasizing key performance indicators and overall temperature behavior, are highlighted. The temperature sensors depict component behavior as follows: (sp1) capacitor at battery port C_{batt}, (sp2) inductor L, (sp3) inductor shunt S_{ind}, (sp4) reference temperature ϑ_{ext}, (sp5) MOSFET M_2 and (sp6) capacitor at applied port C_{app}. Since the color table in chosen to focus on hot spot evaluation with respect to varying heat loss distribution, each use case follows its own coloration. Temperature limits are visible within the temperature evaluation box in terms of the maximum (max, red cross), minimum (min) and average (avg) indicators. The stationary temperature distributions during the two previously identified use-case of interest for the respective charge and discharge scenarios are presented in Fig. 6 along with their respective model replicas.

The hottest spots are visible during discharge operation at MOSFET M_2 (sp1,max) and during charge operation at MOSFET M_3 (max). The average experimental temperature along the converter board varies roughly around 45.0 °C in both use-cases, while the local maximal experimental temperature is at 128.0 °C during discharge operation and 100.0 °C during charge operation. The maximal simulated temperature in the charge use-case scenario is 101 °C and the maximal simulated temperature in the discharge use-scenario is up to 133 °C, both at the same MOSFET spots. The average temperature level of the converter board in the charge use-case scenario is 51.6 °C, and the average temperature level in the discharge use-case scenario is 60.9 °C. Although accurate predictions are made for local hot spots, the mean temperature is overestimated.

The efficiency during discharge and charge cases strongly differs due to the converter configuration. The MOSFET, shunt and inductor locations mostly generate heat, while heat is significantly dissipated along the applied port and backplane. The highest temperature hotspots vary with respect to the operation mode: M_2 during charge buck mode and M_3 during discharge boost mode. When the converter battery and applied voltage are equal, a superimposed switching process and accompanied heat generation are visible, i.e. at MOSFET M_2 and M_4 during charge operation. Similarly, a superimposed effect is to be expected at MOSFET M_1 and M_3 during discharge when the voltage levels at the input and output voltages are equal. The measured temperature rise at the cooling block is scaled due to the heat loss of roughly 40 W during charge and roughly 50 W during discharge operation. While the temperature sensor measurements on the cooling block differ with respect to energy flow, the temperature sensor measurement at the bottom of the converter is similar in both cases. The deviation of the average simulated temperature to the experiment readings is more pronounced during the discharge case than during the charge case. While the temperature levels at the backplane location are slightly underestimated during the charge case, an overestimation is visible at the same location during the discharge case. The deviation at all converter components is provided in Appendix A.2.

3.3. Step 3: Evaluate the base-case performance metrics at hot spots

The base-case module design is examined in terms of temperature levels during cyclic operation at an initial and intermediate cycle with 2.0 kW (flexibility case) and 4.8 kW (worst-case) discharging and 0.8-kW charging power. A constant system power output operation is chosen with respect to the constant converter current and voltage operation. Since the converter prototype is not able to provide the power level to reach 4.8 kW due to electrical or thermal overload, the virtual converter is modeled at 95% electrical efficiency with roughly 50 W total heat dissipation in that case, while a temperature distribution according to the discharge use-case during the experiment is mimicked.

A constant power output operation is modeled at the battery pack with a configuration of 1p12s, 12 battery cells connected in series. While the power output of the system is constant, input power and current have nonlinear profiles with respect to the varying SoC of the incorporated battery model and series connection of the battery cells. Considering a nominal constant power rate of 1.0 P-rate in association with a full battery system's discharge/charge duration of 1.0 h, the system was driven at a power rate of 1.4 P-rate during discharge and a power rate of 0.3 P-rate during charge operation. Therefore, the discharge profile is more electrically demanding than the charge profile with respect to the battery pack, but the thermal impact of the converter is increased during charging due to its longer continuous operation. Li et al. (2022) reported in their study by comparing experimental tests on cell and pack level that the total heat dissipated by each cell in the battery pack during charge or discharge operation remains quantitatively the same, either with 1 C-rate constant current or with 1 P-rate constant power, as the total amount of energy throughput is roughly the same. Hence, we can directly compare constant power mode and constant current mode in terms of heat generation and temperature magnitudes reported in the literature.

The simulated transient temperature rise distribution (K) within the BaSyMo is shown for the battery pack and the back-plane next to the converter during two consecutive discharge/charge cycles in Fig. 7. The

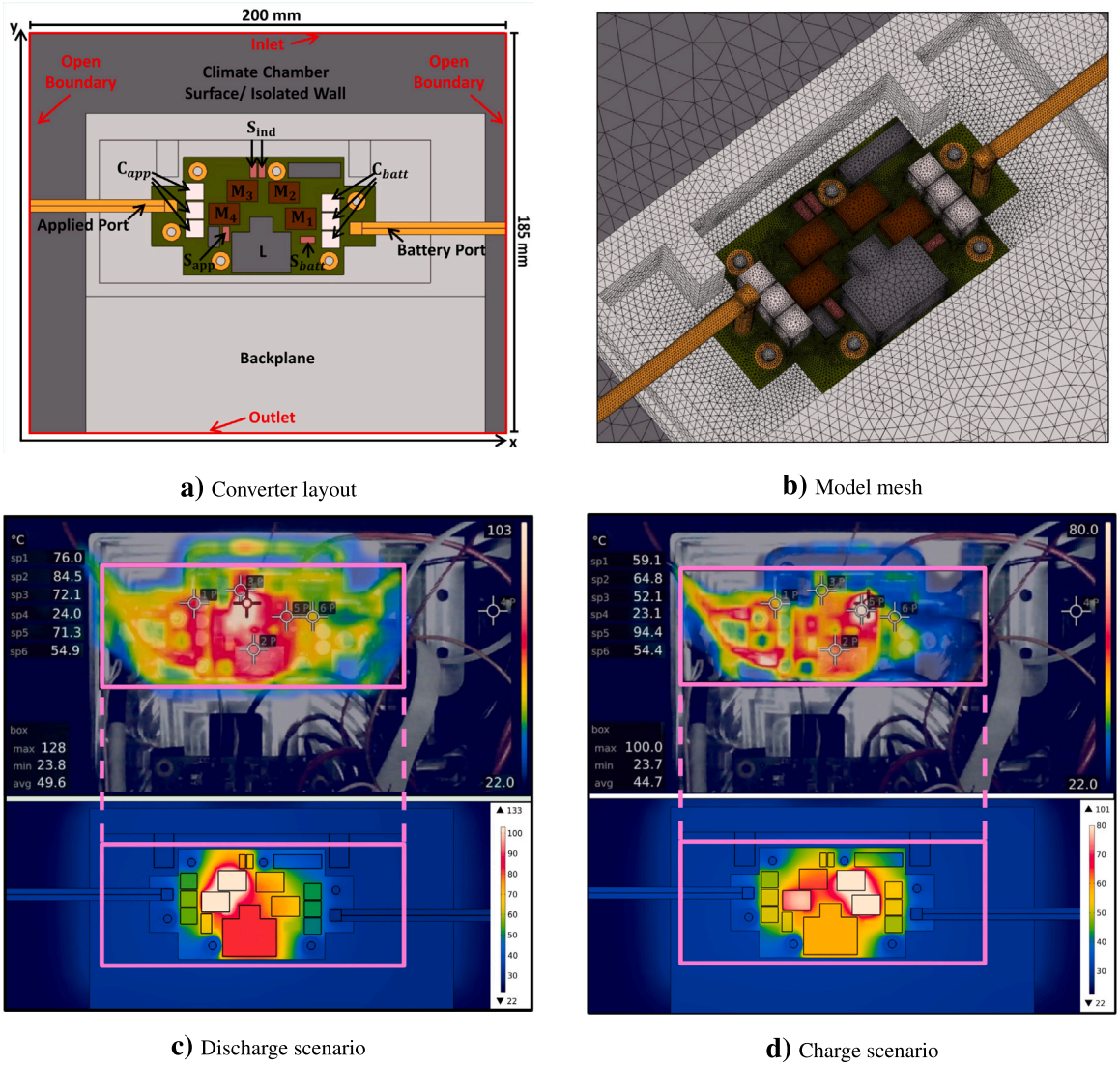

Fig. 6. The converter layout (a) is illustrated along with the tetrahedral mesh triangulation (b) for the numerical approach. The experimental and virtual stationary temperature distribution (°C) are shown during (c) discharge boost operation at the state: [28.68 V, 50.06 V, 19.25 A, −10.06 A] and (d) charge buck operation: [29.87 V, 10.17 V, −5.47 A, 19.91 A].

worst-case condition is reached, when both, the battery pack and the converter, are operated at the most demanding state at the end of the intermediate discharge phase, as depicted in Fig. 8.

The maximum temperature rise at the battery pack at the end of discharge within the intermediate cycle is simulated to be at 24.0 K at stack 6/7 during BaSyMo operation in comparison to a minimal rise of 14.0 K at stack 1/12. There is a strong difference in the thermal behavior of the internal and exterior battery cells of the pack. Ren et al. (2023) reported with decreasing battery temperature level an increase in reversible heat generation is visible. This effect might be visible in the case of high temperature differences, temperature levels far below 22 °C ambient temperature and roughly 0.5 P-rate or below, but not in the current use-case scenario. Hence, the major influence is caused by heat being dissipated differently. From comparison with the heat propagation pattern from previous work (Liebig et al., 2020), we suggest the interior cell dissipates heat mainly by convective cooling on the top terminal and side short surfaces. The exterior cell's longitudinal surface is directly connected to the pack casing end plate, which additionally boosts the cooling effect.

The maximal temperature rise at the converter at the end of discharge in the intermediate cycle is estimated to be 133 K. The temperature rise differs between the discharge test-case (in Fig. 6) and the simulated worst-case condition (in Fig. 8) by up to 22 K. This deviation shows that the maximal temperature magnitude at the MOSFET location is highly sensitive to environmental conditions. In comparison to real-world applications, however, this worst-case temperature level is not far off as it is located at the switching location, which allows a temperature level up to 150 °C (Linear Technology/Analog Devices, 2018). In that case, the converter operation might be thermally limited under the harsh conditions. Either a concept for thermal derating or active cooling needs to be considered, if the same system output is required for the converter application.

The temperature rise distribution evaluated at the backplane is within the range up to 17.0 K. In real-world application, this temperature value is relevant, since it is the maximal temperature value that is measurable on the entire surface of the battery system casing. The maximum safe temperature for a device that humans are allowed to touch without additional safety measures is typically around 50 °C (ISO, 2006). With roughly 40 °C on a metal surface, skin burn is not an issue. However, when the environment temperature is increased, there might be a need to reevaluate the threshold. Mimicking the temperature distribution at the examined operation state is done appropriately, since the temperature distributions of the backplane mainly

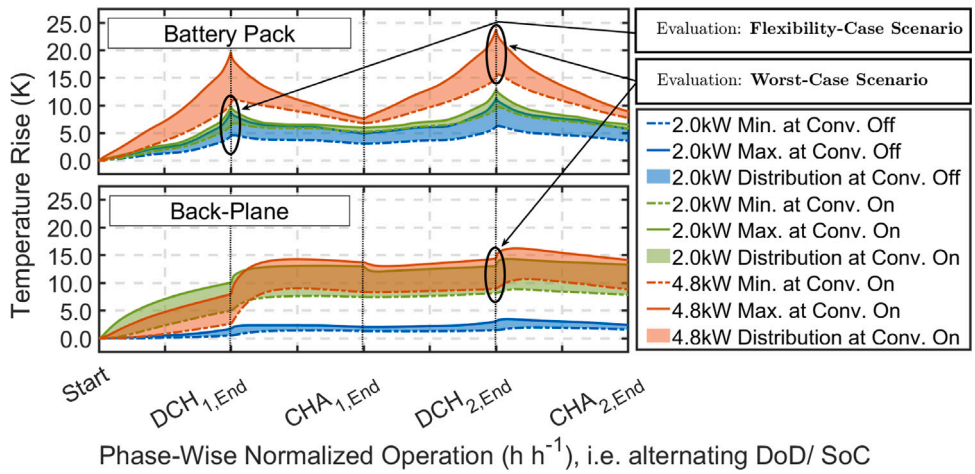

Fig. 7. Simulated temperature rise distribution (K) at cyclic operation with 2.0 kW/4.8 kW discharging and 0.8 kW charging power as a function of phase-wise normalized time (hh^{-1}) at the inlet velocity of $v_{in} = 0.1$ m s^{-1} and environment temperature $\vartheta_{ext} = 22.0$ °C.

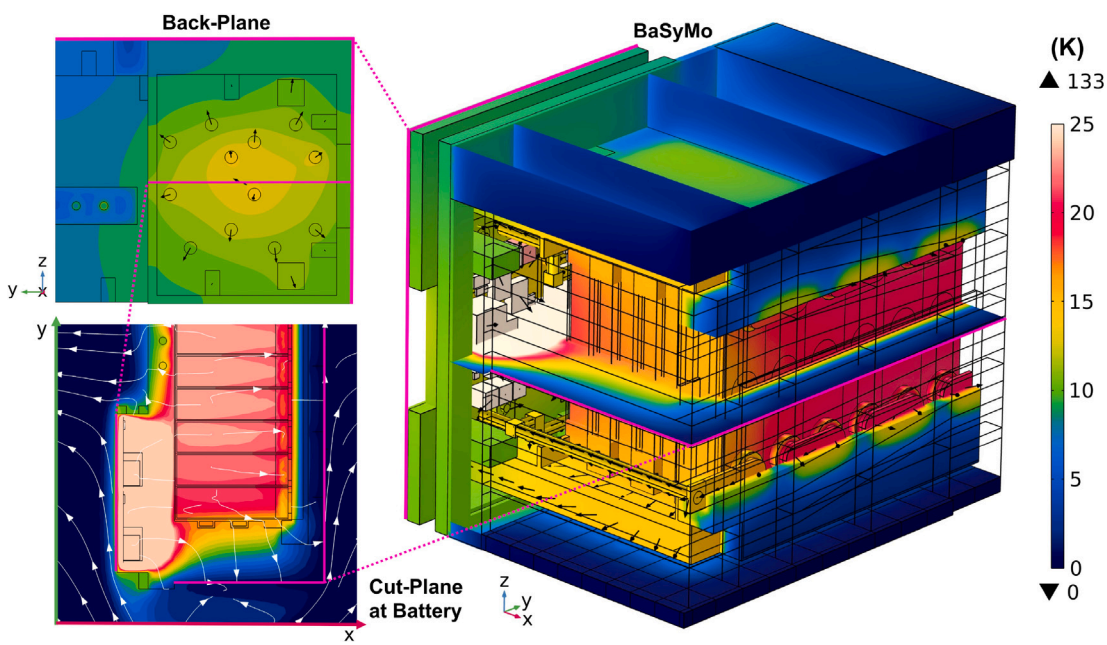

Fig. 8. Several perspectives of the temperature rise distribution (K) of the system design with focus on the battery pack and the back-plane at the end of 4.8 kW discharge-operation during the intermediate cycle; normalized air-stream velocity and thermal gradients are a guide for the eye.

overlap in both analyzed scenarios. Heat flow patterns at the worst-case conditions suggest that convective cooling at the back-plane is the dominant cooling mechanism in this scenario, which can be seen by gradients at the interconnects and the back-plane. However, elevated temperatures by a few degrees are visible in the worst-case scenario in comparison to the flexibility scenario after the initial discharge phase.

Overall, simulated temperature distributions show that the discharge operation is more demanding than the charge operation with respect to the battery pack, but the thermal impact of the converter is increased during charging due to its longer continuous operation. The temperature of the battery pack is lower than the maximal temperature of charge and discharge operation defined by the manufacturer, which suggests safe operation within the whole operation window. While the power output of the system is constant, input power and current have nonlinear profiles in relation to the varying state of charge of the incorporated battery model. With decreasing state-of-charge an increasing current, and a proportional increase in heat generation is simulated. Similar cell behavior is known from a study by Kim et al. (2013). In the current case during discharge operation, increased temperature rise is simulated, when the battery pack state of charge is below the 10% SoC threshold, which correlates to an open-circuit potential of roughly 40.5 V. Hence, state of charge levels below the threshold should be omitted to avoid increased heat generation and a proportional temperature increase or a controller must be considered that is able to cope with the dynamic current (Li et al., 2022).

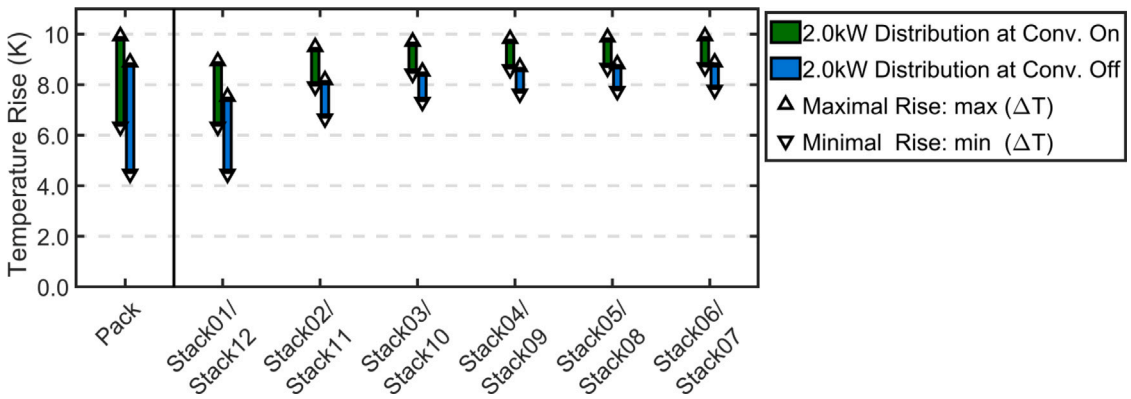

Fig. 9. Battery pack temperature rise distribution (K) of operation versus conventional usage at the end of discharge at the initial cycle.

3.4. Step 4: Evaluate the potential alternative designs - Flexibility as an option

The flexibility scenario is further examined and discussed in the upcoming section on alternative design evaluation. The battery system module operation with the use of the converter array is compared with the conventional usage of the battery pack without voltage adjustment in the flexibility scenario with 2.0 kW discharging and 0.8 kW charging power, as depicted in Fig. 9.

The temperature rise distributions at the end of discharge within the initial cycle vary with respect to the battery pack as follows: 6.2 K minimal rise at stack 1/12 to 10.1 K maximal rise at stack 6/7 during BaSyMo operation in comparison to 4.2 K minimal rise at stack 1/12 to a maximal rise of 9.0 K at stack 6/7 during conventional usage. Similar to the previous use case, one reason for a temperature difference between interior and exterior battery cells is suggested to be convective cooling. However, a constant off-set of increased temperature is visible in the BaSyMo scenario. The reason might be an increased battery pack current, which balances the converter energy loss under the same power demand. An increased impact during long operation is visible and might negatively influence the battery pack operation. In comparison to the conventional use-case, there is a higher temperature rise at the outside lying battery cell but a more uniform temperature rise distribution within the battery pack due to the converter impact. Moreover, during conventional use of the battery pack, heat is propagated towards the converter array, such that it acts as additional passive cooling but increases the thermal nonuniformity of the battery pack. Even though the converter is not in use, this is seen by a temperature increase up to 2.0 K.

3.5. Insights by the design evaluation

The performance analysis for the modular battery system design is presented in this section. Predictions of the battery system model temperature states within the analyzed technological case studies are within a valid range compared to those benchmarks reported in the literature. The converter, however, might be driving in limiting conditions when driven at exceedingly high temperature levels.

Fig. 10 summarizes attributes in this study that focus on cell and a modular system design with finalized results for each system criteria.

Altogether, the battery pack can operate in a safe range within the base-case system design with respect to assessed technological use-case scenarios, while the converter configuration might be limited. Safety can be maintained by the system design, while durability might be reduced due to permanent thermal feedback from the converter array. Moreover, cost could be maintained with the simple passive cooling design, while “easy-to-use” and “flexibility” would increase with the system design. Flexibility can even be considered as an option when the battery voltage window fits the application’s needs.

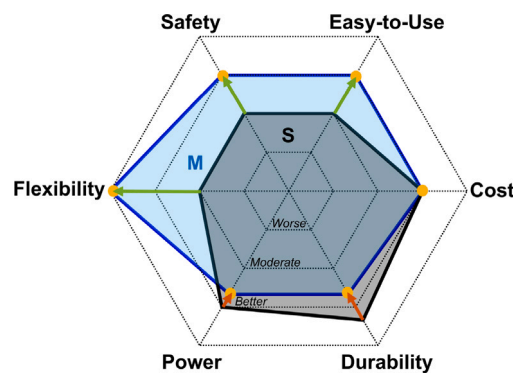

Fig. 10. Final score: Base-case design in comparison to a conventional system based on a Graphite-NMC cell type.

The major result of the converter performance analysis is that it needs to operate at 95% efficiency or below a heat loss of roughly 50 W in order to work thermally stable in the base-case design. This constrains the overall power output of the modular system in comparison to a conventional system, but allows it to provide stable power even at low SoC of the battery pack and limits the thermal overload at the converter components, since the module casing is able to passively cool the converter without excessive temperature levels at the exterior surface of the module casing. Under the assumption of this condition, a maximal temperature rise of 24 K was simulated at 4.8 kW discharge operation at the battery pack, which can be considered the most demanding technological use-case scenario for the present design. Although, the influence of cooling by convection is limited in decreasing the temperature levels of components within the battery system design, the temperature of the battery pack is lower than the maximal temperature of charge and discharge operation defined by the manufacturer. Hence, the base-case design performs better with respect to the safety property in comparison to conventional graphite/NMC-type systems since it can maintain temperature limits, while the modular nature of the design allows for the separate thermal impact of different modules. The behavioral system model shows that the converter might influence the battery pack service-lifetime expectancy negatively with regard to two distinctive systematic thermal sources: increased battery current offsets converter energy loss and leads to a direct increased temperature magnitude at all battery cells and a direct thermal impact at the exterior battery cells. While the first is related to decreased overall energy throughput and power supply as well as a higher overall

battery pack temperature magnitude, the second source is related to the system design layout and has shown minor influence in the base-case design. In the proposed design, the battery pack even benefited from a more uniform temperature distribution.

While our research provides valuable insights, we acknowledge certain limitations and unexplored areas:

- Battery Chemistry Diversity: Our research primarily focuses on Lithium-Ion Batteries (LIBs). However, different battery chemistries exhibit unique thermal behaviors. Future investigations should explore how our framework applies to these alternative chemistries.
- Real-World Operating Conditions: While our simulations assume nominal operating conditions, real-world battery systems operate in diverse environments—ranging from temperature extremes to varying humidity and altitude. Understanding the impact of these variations on thermal management remains an exciting avenue for further study.
- Topology Exploration: Although we examine the present converter topology, our study does not exhaustively cover all possibilities. Investigating additional topologies would enrich our understanding and offer new insights.
- Safety Mechanisms and BTMS: Safety mechanisms, including overcurrent protection and cell balancing, warrant further research. Additionally, exploring an active BTMS could enhance durability, albeit with cost considerations.
- Model Validity and Generalizability: Our study's model relies on simulation data from validated component models. While not capturing all real-world complexities, it provides a solid foundation. Importantly, the methodology is not limited to a specific design—it remains adaptable and applicable.
- Operational Factors and Technological Implications: Our focus on technological implications means that certain operational factors might not be fully explored. Future research could explore these aspects, enhancing more practical applicability.

4. Model verification

The models used to predict the performance of the primary system components, the prismatic graphite-NMC type battery cell and the converter prototype, are examined with respect to the plausibility of the model performance. A set of validation experiments has been performed to calibrate the model parameters to reasonably predict the characteristics of both components. The calibrated models are then used to predict the performance of the system model following the base-case design provided in Section 2.3. The plausibility of the system model study is examined with respect to the chosen spatial mesh configuration.

The model for the graphite-NMC cell was validated against experimental data of a 40 Ah prismatic cell presented in Refs. Liebig et al. (2019b, 2020). For details on the electrochemical model equations and parameterization, the reader is referred to the study (Liebig et al., 2019b) by Liebig et al. To make sure the electrochemical model is correct, it is compared to data from experiments that show charge and discharge phases at different C-rates up to 2.0 C and an ambient of 25 °C. As can be seen in the cell voltage and temperature validation sections in Ref. Liebig et al. (2019b), both heuristic output quantities can be predicted reasonably well. Furthermore, the spatial thermal behavior of the prismatic cell and its nearby environment was investigated in Ref. Liebig et al. (2020). It was determined that the model accurately predicted the distribution of temperature beyond the prismatic cell case.

The power electronics model is a simplified virtual representation of the chosen converter design. Components of the represented converter design are considered that have thermally significant behavior during operation. The heat loss parameterization of the converter prototype is performed based on the evaluation of an inverse heat transfer problem (IHTP) of thermophysical properties and source terms, since the converter components are complex and vary heavily in terms of heat generation and temperature levels at different locations on the printed circuit board (PCB) during testing (Ozisik, 2000). The detailed problem statement and model parameter results from the IHPT evaluation are shown in Appendix A.2. The converter model accuracy and thermal results are discussed in Section 3.2 along with the experimental performance evaluation.

The system model has an average skewness of 0.62 and an average condition number of 0.75 for solid components and their surfaces. The criteria "skewness" evaluates the anisotropy of angles within mesh elements, whereas the quantity "condition number" qualifies the matrix isometric transformation properties of the actual elements; both in comparison to an ideal tetrahedral element with both equally adjusted angles and a maximal condition number. Mesh refinement is considered in areas with more detailed contours like the converter components, battery components and copper connections. The casing surface is refined with boundary layers with regards to the fluid flow environment. To understand the sensitivity of the evaluated thermal results based on the chosen spatial mesh discretization, mean temperature profiles at the battery pack are examined. The influence of the mesh is examined in a simplified test comparing the influence of the final mesh with that of a twofold coarsened mesh. The deviation remains below 0.1 K absolute error on the evaluated stack and battery pack volumes during the worst-case condition cycle. Hence, the impact of numerical errors is assumed to be negligible in each evaluated use-case. The system model mesh configuration that is used during the study and the submodel mesh variants are depicted in Appendix A.1.

5. Conclusion

In this study, we introduce a comprehensive simulative design engineering framework for the virtual assessment of lithium-ion battery systems. Our primary focus is to support design research under limiting conditions in the early phases of development. Our contributions are threefold:

- Simulative engineering framework: Our framework serves as a powerful tool, allowing engineers to simulate various scenarios and evaluate battery system designs. Thereby, enhancing efficiency of design exploration and decision-making.
- Thermal Evaluation of the BaSyMo Design: By understanding temperature effects on key components, we enhance our system-level insights. Our converter performance analysis reveals that maintaining at least 95% efficiency and minimizing heat loss (below 50 W) ensures thermal stability within the base-case design. Simulated results demonstrate a maximal temperature rise of 24 K during a demanding 4.8 kW battery pack discharge. The battery pack remains below manufacturer-defined maximum temperatures, emphasizing safety. Passive cooling mechanisms within the module casing effectively prevent converter component thermal overload.
- Reliable Component Assessment: We rigorously assess the battery and dc-to-dc converter, ensuring their reliability and performance. Our findings align with empirical data from experiments and existing literature, reinforcing the validity of our approach.

In summary, our work bridges theory and practical design, providing valuable insights for the advancement of battery technology. However, we acknowledge limitations such as battery chemistry diversity, real-world operating conditions, topology exploration, safety mechanisms, model validity, and operational factors. The methodology is adaptable and applicable, but there are still relevant factors that could be evaluated in the future work.

Abbreviations

The following abbreviations are used in this manuscript:

0D	Zero-dimensional
3D	Three-dimensional
BaSyMo	Battery system for modularity
BTMS	Battery thermal management system
CFD	Computational fluid dynamics
DoF	Degree of freedom
DoD	Depth of discharge
FEM	Finite-element method
LFP	Iron-phosphate positive electrode material
LIB	Lithium-ion battery
IHTP	Inverse heat transfer problem
NMC	Nickel manganese cobalt positive electrode material
MOSFET	Metal–oxide–semiconductor field-effect transistors
PCB	Printed circuit board
P2D	Pseudo two-dimensional
SoC	State of charge
SoH	State of health
SA	Simulated annealing

CRediT authorship contribution statement

Gerd Liebig: Writing – original draft, Visualization, Validation, Software, Methodology, Investigation, Formal analysis, Data curation, Conceptualization. **Stefan Geißendörfer:** Writing – review & editing, Supervision, Methodology, Investigation, Conceptualization. **Frank Schuldt:** Writing – review & editing, Supervision, Project administration, Conceptualization. **Karsten von Maydell:** Writing – review & editing, Supervision, Funding acquisition.

Declaration of competing interest

The authors declare that they have no known competing financial interests or personal relationships that could have appeared to influence the work reported in this paper.

Data availability

Data will be made available on request. Models cannot be provided.

Acknowledgments

The authors acknowledge O. Zahid for his master's thesis work on the thermal modeling of earlier design iterations of the BaSyMo concept. Moreover, the authors appreciate the suggestions and fruitful conversations regarding the battery and converter characteristics that they received from A. Bornemann, L. Uhse, G. Bremer, J.G. Hornung and O. Zahid. The authors gratefully acknowledge the financial support provided by BMWi, the German Federal Ministry of Economic Affairs and Energy, for funding of the project BaSyMo (FKZ: 03ET6087I). We like to thank our project partners for their contributions: ElringKlinger AG, University of Stuttgart - Institute for Engineering Design and Industrial Design, PHOENIX CONTACT GmbH & Co. KG, Sensor-Technik Wiedemann GmbH, Alfred Kärcher SE & Co. KG und Hafen- und Industrietechnik GmbH.

Fundings

This research, "BaSyMo" (FKZ: 03ET6087I), was funded by the Federal Ministry of Economic Affairs and Energy (BMWi).

Appendix

A.1. FEM discretization and solving

In this work, FEM is applied to discretize the underlying equations of the presented model variants by using the commercial solver COMSOL Multiphysics® 5.6. The individual spatial discretization is considered for the different length scales represented at each submodel referred to within the study and shown in Table A.1.

The solving process is based on the COMSOL Multiphysics® 5.6 built-in multifrontal massively parallel sparse direct solver (MUMPS) with a relative and absolute tolerance of 10^{-3} at a maximal step-size of 1 s. All models are computed on Intel® Core™ i7-10700K CPU @ 3.80 GHz with 32 GB RAM.

A.2. 3D converter model parameterization

The problem statement is formulated as follows: Given a vector of measured temperature data $\vec{\vartheta}_{meas}$ at different locations within the test set-up in reality and a vector of parameters $\vec{P}$ with the relation $f(\vec{P}) = \vec{\vartheta}_{sim}$, where f is without further requirements. Find $\vec{P}^*$ such that $f(\vec{P}^*) = \vec{\vartheta}^*_{sim} \approx \vec{\vartheta}_{meas}$, i.e., a relatively similar thermal behavior at the collocated locations within the virtual model environment and real test set-up is derived. An iterative estimation is performed in the minimization with the objective weighted least squares function stated as follows:

$$S(\vec{P}) = \frac{1}{2}\sum_{m\in M} w_m \left(\vartheta_{m,meas} - f_m(\vec{P})\right)^2 = \frac{1}{2}[\vec{\vartheta}_{meas} - \vec{\vartheta}_{sim}]^T W [\vec{\vartheta}_{meas} - \vec{\vartheta}_{sim}] \tag{A.1}$$

where W is a diagonal matrix with predetermined weighting coefficients,

$\sum_{m\in M} w_m = 1, w_m > 0 \ \forall m \in M$, involving M temperature measurements (Ozisik, 2000).

The Eq. (A.1) defines the cost function S in terms of a converter model evaluation function f. This is a model version of the system model that is based on the governing equations and boundary conditions described in the modeling approach for the test setup. The physical setting comprises a time invariant reformulation of the Eqs. (1) to (12) with a restriction on the converter geometry and attached cooling block, aka system casing. The modeled components comprise one communication plug, one fuse, one inductor casing, one inductor kernel, six capacitors, four MOSFETs and four shunts due to their thermal significance. The PCB is modeled as a thermally thin layer with orthotropic thermal conductivities. The component's heat capacity, density and thermal conductivity are chosen from well-known materials in the literature. Only the thermal conductivities of the PCB board are considered to be calculated in the optimization process, along with the source terms. Altogether, the following set of parameters is chosen for the iterative process.

$$\vec{P} = [Q_L, Q_{S,batt}, Q_{S,ind}, Q_{S,app}, Q_{C,batt}, Q_{C,app}, Q_{M,1}, Q_{M,2}, Q_{M,3}, Q_{M,4}, k_{pcb,th}, k_{pcb,in}] \tag{A.2}$$

As of version 2017b, the optimization routine can be run on MATLAB (United States, Natick) and is based on the Simulated Annealing (SA) algorithm from the Global Optimization toolbox (The MathWorks Inc., 2020; Ingber, 1995). The heat source parameters of the converter components are implemented current-controlled within the module behavioral model such that heat at the converter is only generated when the virtual converter model is actively operated at the predefined electrical conditions. The material data derived in the charge use-case is chosen to be fixed in the optimization process of the discharge use-case since the material properties are expected to be independent of the operation.

Table A.1
FEM mesh configurations.

Model	Geometry	Vertices	Elements[a]	Method	∑ DoF[b]
P2D (Validation)	Electrode stack	41	40	FEM[c]	1108 (plus 10 internal DoFs)
P2D+3D (Validation)	Prismatic cell	8625[d]/74,707[e]	63,505[d]/368,531[e]	FEM[f]	81,182 (plus 432,851 internal DoFs)
3D (Validation)	Converter	52,247[d]/226,546[e]	203,754[d]/ 1,150,801[e]	FEM[g]	344,280 (plus 1,534,695 internal DoFs)
P2D+3D (Study)	System	98,224[d]/392,696[e]	422,826[d]/ 2,044,280[e]	FEM[g]	613,216 (plus 2,376,550 internal DoFs)

[a] User defined settings incorporating a COMSOL built-in meshing algorithm.
[b] Total degrees of freedom for the entire model.
[c] Ref. Liebig et al. (2019b).
[d] In solid domains.
[e] In fluid domains.
[f] Tetrahedral elements, Ref. Liebig et al. (2020).
[g] Pyramid, prism and tetrahedral elements.

Table A.2
The heat, thermal and deviation properties of the converter behavior replication process.

Meaning	Symbol	Experimental temperature T_{exp} (°C)	Heat source density[a] Q_{sim} (W m^{-3})	Average simulated temperature T_{sim} (°C)	Absolute deviation $T_{exp} - T_{sim}$ (°C)
Charge case with cost $f = 7.62$ for weighting coefficients $\vec{w}$[b]					
Inductor coil	L_{coil}	64.9	267,630	58.3	6.6
Shunt	S_{batt}	54.4	93,137	56.9	−2.5
Shunt	S_{app}	64.9	7,142,200	59.3	5.6
Shunt	S_{ind}	52.1	1,141,500	51.7	0.4
Capacitor	C_{batt}	54.4	129,880	51.8	2.6
Capacitor	C_{app}	58.9	275,600	59.3	−0.4
MOSFET	M_1	94.1	1,773,700	87.3	6.8
MOSFET	M_2	100.0	2,334,800	92.2	7.8
MOSFET	M_3	64.9	335,720	62.4	2.5
MOSFET	M_4	75.0	1,225,900	73.5	1.5
Casing close to battery port	$T_{batt,casing}$	25.9	–	29.6	−3.7
Casing centered at back-plane	$T_{back,casing}$	32.8	–	31.6	−1.2
Casing close to applied port	$T_{app,casing}$	28.7	–	30.2	1.5
Discharge case with cost $f = 6.25$ for weighting coefficients $\vec{w}$[b]					
Inductor coil	L_{coil}	84.5	697,190	82.1	2.4
Shunt	S_{batt}	54.8	6,791	59.6	−4.8
Shunt	S_{app}	84.5	3,686,300	79.4	5.1
Shunt	S_{ind}	72.2	1,088,000	71.6	0.6
Capacitor	C_{batt}	54.8	173,170	50.7	4.1
Capacitor	C_{app}	76.0	26,542	79.4	−3.4
MOSFET	M_1	75.7	699,340	71.5	4.2
MOSFET	M_2	75.7	852,760	71.8	3.9
MOSFET	M_3	128.0	2,566,700	123.3	4.7
MOSFET	M_4	128.0	2,857,600	120.8	7.1
Casing close to battery port	$T_{batt,casing}$	29.2	–	31.3	−2.1
Casing centered at back-plane	$T_{back,casing}$	33.4	–	34.1	−0.7
Casing close to applied port	$T_{app,casing}$	30.6	–	32.6	−2.0

[a] Refined.
[b] $\vec{w} = (w_i)$, $w_i = \frac{2}{9}$ for $i = \{1, 2, 3\}$ and $w_i = \frac{1}{30}$ for $i = \{4, \dots, 13\}$.

Table A.3
The considered thermophysical properties of the virtual converter components.

Meaning	Symbol	Reference bulk	Reference surface[a]	Measured volume v (mm^3)	Density ρ (kg m^{-3})	Heat capacity C_p (J kg^{-1} K^{-1})	Thermal conductivity k (W m^{-1} K^{-1})	Emissivity ϵ
MOSFET	$M_{1/2/3/4}$	Silicon glass	Black, heat-resistant	702.7	2203.0	703.0	1.38	0.92
Capacitor	$C_{batt/app}$	Aluminum	Unmodified	776.1	2700.0	900.0	238.0	0.09
Shunt	$S_{batt/app/ind}$	Steel	Oxidized	20.4[b] 29.9[c]	7850.0	475.0	44.5	0.74

(continued on next page)

Table A.3 (*continued*).

Meaning	Symbol	Reference bulk	Reference surface[a]	Measured volume v (mm^3)	Density ρ (kg m^{-3})	Heat capacity C_p (J kg^{-1} K^{-1})	Thermal conductivity k (W m^{-1} K^{-1})	Emissivity ϵ
Inductor coil	L_{coil}	Copper	Shiny	4195.4	8960.0	385.0	400.0	0.07
Inductor case	L_{case}	Steel	Black, Shiny	5507.5	7850.0	475.0	44.5	0.87

[a] Emissivity reference taken from OptrisGmbH (2023).
[b] With respect to $S_{batt/app}$.
[c] With respect to S_{ind}.

Table A.4
The considered thermophysical properties of the converter's PCB.

Meaning	Symbol	Reference bulk	Reference surface[a]	Thickness L (mm)	Density ρ (kg m^{-3})	Heat capacity C_p (J kg^{-1} K^{-1})	Thermal conductivity k (W m^{-1} K^{-1})	Emissivity ϵ
Printed circuit board	PCB	FR4	Green, laminated	1.83	1900.0	1369.0	3.39[b,c] 0.27[b,d]	0.94

[a] Emissivity reference taken from OptrisGmbH (2023).
[b] Refined.
[c] || (in-plane).
[d] ⊥ (through-plane).

The experimental results, the initially chosen set of parameters used for the optimization procedure and the final set of refined converter model parameters are presented in Table A.2. The fixed thermophysical properties of the mounted converter components are chosen with respect to their main material property and are presented in Table A.3. The converter's PCB thin-sheet anisotropical thermal conductivities are refined based on the optimization implementation for the discharge case. The final parameter dataset is presented in Table A.4.

References

Achim, K., Heimes, H.H., Offermanns, C., Sasse, K., Frieges, M.H., Späth, B., 2022. Domain based product architecture approach for innovative battery system design. In: 2022 International Symposium on Electromobility. ISEM, pp. 1–6. http://dx.doi.org/10.1109/ISEM55847.2022.9976814.

Alatai, S., Salem, M., Ishak, D., Das, H.S., Alhuyi Nazari, M., Bughneda, A., Kamarol, M., 2021. A review on state-of-the-art power converters: Bidirectional, resonant, multilevel converters and their derivatives. Appl. Sci. 11 (21), http://dx.doi.org/10.3390/app112110172, URL https://www.mdpi.com/2076-3417/11/21/10172.

Arora, S., 2018. Selection of thermal management system for modular battery packs of electric vehicles: A review of existing and emerging technologies. J. Power Sources 400, 621–640. http://dx.doi.org/10.1016/j.jpowsour.2018.08.020.

Astaneh, M., Andric, J., Löfdahl, L., Stopp, P., 2022. Multiphysics simulation optimization framework for lithium-ion battery pack design for electric vehicle applications. Energy 239, 122092. http://dx.doi.org/10.1016/j.energy.2021.122092, URL https://www.sciencedirect.com/science/article/pii/S0360544221023409.

Bandhauer, T.M., Garimella, S., Fuller, T.F., 2011. A critical review of thermal issues in lithium-ion batteries. J. Electrochem. Soc. 158, R1. http://dx.doi.org/10.1149/1.3515880.

Brand, M., Gläser, S., Geder, J., Menacher, S., Obpacher, S., Jossen, A., Quinger, D., 2013. Electrical safety of commercial Li-ion cells based on NMC and NCA technology compared to LFP technology. World Electr. Veh. J. 6 (3), 572–580. http://dx.doi.org/10.3390/wevj6030572, URL https://www.mdpi.com/2032-6653/6/3/572.

Chang, L., Chen, W., Mao, Z., Huang, X., Ren, T., Zhang, Y., Cai, Z., 2023. Experimental study on the effect of ambient temperature and discharge rate on the temperature field of prismatic batteries. J. Energy Storage 59, 106577. http://dx.doi.org/10.1016/j.est.2022.106577, URL https://www.sciencedirect.com/science/article/pii/S2352152X2202566X.

Chen, C.-H., Planella, F.B., O'Regan, K., Gastol, D., Widanage, W.D., Kendrick, E., 2020. Development of experimental techniques for parameterization of multi-scale lithium-ion battery models. J. Electrochem. Soc. 167 (8), 080534. http://dx.doi.org/10.1149/1945-7111/ab9050.

Dokić, B.L., Blanuša, B., 2014. Power Electronics; Converters and Regulators, third ed. Springer International Publishing.

Epp, A., Sauer, D.U., 2021. Multiperspective optimization of cell and module dimensioning for different lithium-ion cell formats on geometric and generic assumptions. Energy Technol. 10 (3), 2100874. http://dx.doi.org/10.1002/ente.202100874, arXiv: https://onlinelibrary.wiley.com/doi/pdf/10.1002/ente.202100874, URL https://onlinelibrary.wiley.com/doi/abs/10.1002/ente.202100874.

Frith, J.T., Lacey, M.J., Ulissi, U., 2023. A non-academic perspective on the future of lithium-based batteries. Nature Commun. 14 (420), http://dx.doi.org/10.1038/s41467-023-35933-2.

Geng, Z., Wang, S., Lacey, M.J., Brandell, D., Thiringer, T., 2021. Bridging physics-based and equivalent circuit models for lithium-ion batteries. Electrochim. Acta 372, 137829. http://dx.doi.org/10.1016/j.electacta.2021.137829, URL https://www.sciencedirect.com/science/article/pii/S0013468621001183.

Graf, C., 2018. Cathode materials for lithium-ion batteries. In: Korthauer, R. (Ed.), Lithium-Ion Batteries: Basics and Applications. Springer Berlin Heidelberg, Berlin, Heidelberg, Germany, pp. 29–41. http://dx.doi.org/10.1007/978-3-662-53071-9_4.

Grey, C.P., Hall, D.S., 2020. Prospects for lithium-ion batteries and beyond—a 2030 vision. Nature Commun. 11 (1), 6279. http://dx.doi.org/10.1038/s41467-020-19991-4.

Hautier, G., Jain, A., Ong, S.P., Kang, B., Moore, C., Doe, R., Ceder, G., 2011. Phosphates as lithium-ion battery cathodes: An evaluation based on high-throughput ab initio calculations. Chem. Mater. 23 (15), 3495–3508. http://dx.doi.org/10.1021/cm200949v.

Ingber, L., 1995. Adaptive simulated annealing (ASA): Lessons learned. Available online: [https://www.ingber.com/asa96_lessons.ps.gz], accessed on 15 March 2024.

2006. ISO 13732-1:2006-Ergonomics of the thermal environment - Methods for the assessment of human responses to contact with surfaces - Part 1: Hot surfaces. Available online: [https://www.beuth.de/de/norm/din-en-iso-13732-1/111624965], accessed on 15 March 2024.

Jokar, A., Rajabloo, B., Désilets, M., Lacroix, M., 2016. An inverse method for estimating the electrochemical parameters of lithium-ion batteries. J. Electrochem. Soc. 163 (14), A2876–A2886. http://dx.doi.org/10.1149/2.0191614jes.

Keyser, M., Pesaran, A., Li, Q., Santhanagopalan, S., Smith, K., Wood, E., Ahmed, S., Bloom, I., Dufek, E., Shirk, M., Meintz, A., Kreuzer, C., Michelbacher, C., Burnham, A., Stephens, T., Francfort, J., Carlson, B., Zhang, J., Vijayagopal, R., Hardy, K., Dias, F., Mohanpurkar, M., Scoffield, D., Jansen, A.N., Tanim, T., Markel, A., 2017. Enabling fast charging – Battery thermal considerations. J. Power Sources 367, 228–236. http://dx.doi.org/10.1016/j.jpowsour.2017.07.009.

Khan, M., Swierczynski, M., Kær, S., 2017. Towards an ultimate battery thermal management system: A review. Batteries 3 (4), 9. http://dx.doi.org/10.3390/batteries3010009.

Kim, U.S., Yi, J., Shin, C.B., Han, T., Park, S., 2013. Modeling the thermal behaviors of a lithium-ion battery during constant-power discharge and charge operations. J. Electrochem. Soc. 160 (6), A990. http://dx.doi.org/10.1149/2.146306jes.

Korthauer, R., 2013. Handbuch Lithium-Ionen-Batterien. Springer Berlin Heidelberg, http://dx.doi.org/10.1007/978-3-642-30653-2.

Li, J., Xu, S., Dai, C., Zhao, M., Wang, Z., 2022. Characteristic prediction and temperature-control strategy under constant power conditions for lithium-ion batteries. Batteries 8 (11), http://dx.doi.org/10.3390/batteries8110217, URL https://www.mdpi.com/2313-0105/8/11/217.

Liebig, G., Gupta, G., Kirstein, U., Schuldt, F., Agert, C., 2019b. Parameterization and validation of an electrochemical thermal model of a lithium-ion battery. Batteries 5 (3), 62. http://dx.doi.org/10.3390/batteries5030062.

Liebig, G., Kirstein, U., Geißendörfer, S., Zahid, O., Schuldt, F., Agert, C., 2020. The impact of environmental factors on the thermal characteristic of a lithium–ion battery. Batteries 6 (1), 3. http://dx.doi.org/10.3390/batteries6010003.

Liebig, G., Kirstein, U., Schuldt, F., Maydell, K., Agert, C., 2019a. Poster: Thermal analysis supporting robust designing of a modular 24–48 V lithium-ion battery system and safety considerations for the integrated components. In: Battery Power Conference. Aachen, Germany.

Linear Technology/Analog Devices, 2018. LT8707 - 80 V synchronous 4-switch buck-boost DC/DC controller with bidirectional capability. Available online: [https://www.analog.com/media/en/technical-documentation/data-sheets/LT8708.pdf], accessed on 15 March 2024.

Lundgren, H., Svens, P., Ekström, H., Tengstedt, C., Lindström, J., Behm, M.a., Lindbergh, G., 2015. Thermal management of large-format prismatic lithium-ion battery in PHEV application. J. Electrochem. Soc. 163 (2), A309–A317. http://dx.doi.org/10.1149/2.09411602jes.

Madani, S.S., Ziebert, C., Marzband, M., 2023. Thermal behavior modeling of lithium-ion batteries: A comprehensive review. Symmetry 15 (8), http://dx.doi.org/10.3390/sym15081597, URL https://www.mdpi.com/2073-8994/15/8/1597.

Marcicki, J., Zhu, M., Bartlett, A., Yang, X.G., Chen, Y., Miller, T., L'Eplattenier, P., Caldichoury, I., 2017. A simulation framework for battery cell impact safety modeling using LS-DYNA. J. Electrochem. Soc. 164 (1), A6440. http://dx.doi.org/10.1149/2.0661701jes.

Nations, U., 2015. Paris agreement. C.N.92.2016.TREATIES-XXVII.7.d..

Newman, J., Tiedemann, W., 1975. Porous-electrode theory with battery applications. AIChE J. 21 (1), 25–41. http://dx.doi.org/10.1002/aic.690210103.

Omariba, Z.B., Zhang, L., Sun, D., 2019. Review of battery cell balancing methodologies for optimizing battery pack performance in electric vehicles. IEEE Access 7, 129335–129352. http://dx.doi.org/10.1109/ACCESS.2019.2940090.

OptrisGmbH, 2023. Basic principles of non-contact temperature measurement. Available online: [https://www.optris.com/de/download/optris-infrarot-grundlagen/], accessed on 15 March 2024.

Ozisik, M.N., 2000. Inverse Heat Transfer. Routledge, http://dx.doi.org/10.1201/9780203749784.

Poblete-Cazenave, M., Pachauri, S., Byers, E., Mastrucci, A., van Ruijven, B., 2021. Global scenarios of household access to modern energy services under climate mitigation policy. Nat. Energy 6 (8), 824–833. http://dx.doi.org/10.1038/s41560-021-00871-0.

Queisser, O., Cloos, L., Boehm, F., Oehler, D., Wetzel, T., 2021. Impact of the level of homogenization in 3D thermal simulation on the internal temperature distribution of Li-Ion battery cells. Energy Technol. 9 (6), 2000915. http://dx.doi.org/10.1002/ente.202000915.

Reiter, C., Lin, X., Schlereth, L.-E., Lienkamp, M., 2019. Finding the ideal automotive battery concept. Forschung Ingen. 83 (4), 817–830. http://dx.doi.org/10.1007/s10010-019-00316-x.

Ren, T., Mao, Z., Chang, L., Chen, W., Xu, J., Zhang, Y., Chen, T., Cai, Z., 2023. Experimental and simulation studies on the thermal characteristics of large-capacity square lithium-ion batteries with low-temperature discharge. Energy Technol. 12 (1), 2300826. http://dx.doi.org/10.1002/ente.202300826, URL https://onlinelibrary.wiley.com/doi/abs/10.1002/ente.202300826.

Rojas, C., Oca, L., Lopetegi, I., Iraola, U., Carrasco, J., 2024. A critical look at efficient parameter estimation methodologies of electrochemical models for Lithium-Ion cells. J. Energy Storage 80, 110384. http://dx.doi.org/10.1016/j.est.2023.110384, URL https://www.sciencedirect.com/science/article/pii/S2352152X23037830.

Rothgang, S., Baumhöfer, T., van Hoek, H., Lange, T., De Doncker, R.W., Sauer, D.U., 2015. Modular battery design for reliable, flexible and multi-technology energy storage systems. Appl. Energy 137, 931–937. http://dx.doi.org/10.1016/j.apenergy.2014.06.069.

Saw, L.H., Ye, Y., Tay, A.A., 2016. Integration issues of lithium-ion battery into electric vehicles battery pack. J. Clean. Prod. 113, 1032–1045. http://dx.doi.org/10.1016/j.jclepro.2015.11.011, URL https://www.sciencedirect.com/science/article/pii/S0959652615016406.

Schlick, T., Hagemann, B., Kramer, M., Garrelfs, J., Rassmann, A., 2012. Zukunftsfeld energiespeicher - Marktpotenziale standardisierter lithium-ionen-batteriesysteme. Available online: [https://fva-net.de/fileadmin/download/E-MOTIVE/20120912_VDMA-Studie_PK_Veroeffentlichung.pdf], accessed on 15 March 2024.

Seider, W., Seader, J., Widegado, S., Gani, R., Ng, K., 2017. Product and Process Design Principles: Synthesis, Analysis and Evaluation, fourth ed. Wiley.

Severns, R.P., Bloom, G.E., 1985. Modern DC-to-DC Power Converter Circuits. Van Nostrand Reinhold Company.

Smith, K., Shi, Y., Wood, E., Pesaran, A., 2016. Presentation: Optimizing battery usage and management for long life. In: Advanced Automotive Battery Conference. Detroit, Michigan, Available online: [https://www.nrel.gov/docs/fy16osti/66708.pdf], accessed on 15 March 2024.

Sutikno, T., Aprilianto, R.A., Purnama, H.S., 2023. Application of non-isolated bidirectional DC–DC converters for renewable and sustainable energy systems: a review. Clean Energy 7 (2), 293–311. http://dx.doi.org/10.1093/ce/zkac070.

The MathWorks Inc., 2020. Simulated annealing. Available online: [https://de.mathworks.com/discovery/simulated-annealing.html], accessed on 15 March 2024.

VDI/VDE, 2021. 2206:2021-11, Development of mechatronic and cyber-physical systems.

Vega-Garita, V., Ramirez-Elizondo, L., Bauer, P., 2017. Physical integration of a photovoltaic-battery system: A thermal analysis. Appl. Energy 208, 446–455. http://dx.doi.org/10.1016/j.apenergy.2017.10.007.

Xi, S., Chang, L., Chen, W., Zhao, Q., Guo, Y., Cai, Z., 2022. Mechanical response analysis of battery modules under mechanical load: Experimental investigation and simulation analysis. Energy Technol. 10 (3), 2100763. http://dx.doi.org/10.1002/ente.202100763, arXiv:https://onlinelibrary.wiley.com/doi/pdf/10.1002/ente.202100763, URL https://onlinelibrary.wiley.com/doi/abs/10.1002/ente.202100763.

Yang, Y., Chen, L., Tong, K., Yang, L., Jiang, K., Kong, Y., Du, X., 2022. Thermal-electrical characteristics of lithium-ion battery module in series connection with a hybrid cooling. Int. J. Heat Mass Transfer 184, 122309. http://dx.doi.org/10.1016/j.ijheatmasstransfer.2021.122309.

Zahid, O., 2018. Three-Dimensional Modelling and Thermal Analysis of a 24–48V Lithium-Ion Battery System Module (Master's thesis). University of Oldenburg.

Zhang, X., Zhang, L., Fung, K.Y., Bakshi, B.R., Ng, K.M., 2020. Sustainable product design: A life-cycle approach. Chem. Eng. Sci. 217, 115508. http://dx.doi.org/10.1016/j.ces.2020.115508.

Zhao, R., Zhang, S., Liu, J., Gu, J., 2015. A review of thermal performance improving methods of lithium ion battery: Electrode modification and thermal management system. J. Power Sources 299, 557–577. http://dx.doi.org/10.1016/j.jpowsour.2015.09.001.

Zubi, G., Dufo-López, R., Carvalho, M., Pasaoglu, G., 2018. The lithium-ion battery: State of the art and future perspectives. Renew. Sustain. Energy Rev. 89, 292–308. http://dx.doi.org/10.1016/j.rser.2018.03.002, URL https://www.sciencedirect.com/science/article/pii/S1364032118300728.